A whole-cortex probabilistic diffusion tractography connectome

Burke Q Rosen[1], Eric Halgren[1,2]
1. Neurosciences graduate program, University of California, San Diego, La Jolla, CA, United States
2. Departments of Radiology and Neurosciences, University of California, San Diego, La Jolla, CA, United States

Keywords: Diffusion MRI, structural connectome, tractography, Human Connectome Project

Abstract The WU-Minn Human Connectome Project (HCP) is a publicly-available dataset containing state-of-art structural, functional, and diffusion-MRI for over a thousand healthy subjects. While the planned scope of the HCP included an anatomical connectome, resting-state functional-MRI forms the bulk of the HCP's current connectomic output. We address this by presenting a full-cortex connectome derived from probabilistic diffusion tractography and organized into the HCP-MMP1.0 atlas. Probabilistic methods and large sample sizes are preferable for whole-connectome mapping as they increase sensitivity to low-probability connections. We find that overall connectivity is lognormally distributed and decays exponentially with tract length, that connectivity reasonably matches macaque histological tracing in homologous areas, that contralateral homologs and left-lateralized language areas are hyperconnected, and that hierarchical similarity influences connectivity. This work helps fulfill the promise of the HCP and will make possible comparisons between the underlying structural connectome and functional connectomes of various modalities, brain states, and clinical conditions.

Introduction

In the 21st century, advances in computation, theory, and neuroimaging have spurred a broad and intense interest in the anatomical connections and physiological correlations among human brain areas. Bivariate functional connectivity has given way to full functional connectomes, the most comprehensive of which may be the WU-Minn Human Connectome Project's (HCP) resting state fMRI dense connectome: a high-resolution summary matrix corticocortical BOLD correlativity during quiescent waking (Van Essen et al., 2013). However, the term connectome was originally coined to mean the full diagram of anatomical connections linking the neuronal elements of the brain (Hagmann, 2005; Sporns, Tononi, & Kötter, 2005). The planned scope of WU-Minn HCP includes a full anatomical connectome (Van Essen et al., 2013; Van Essen & Ugurbil, 2017), and the project has collected, curated, and preprocessed diffusion imaging (dMRI) data for more than a thousand subjects. Despite these intentions and efforts, a structural connectome has to-date not been released for these data. This report seeks to address this omission by presenting a full-cortex anatomical connectome derived from local, probabilistic tractography (Behrens, Berg, Jbabdi, Rushworth, & Woolrich, 2007; Jenkinson, Beckmann, Behrens, Woolrich, & Smith, 2012).

Connectome Features
Probabilistic methodology sensitive to weak connections yielding a fully-populated connectome
Cortex parcellated into the standardized, relatively dense, and functionally relevant HCP-MMP1.0 atlas
Large normative sample size (N = 1,065)
Enables comparison with other measures in the WU-Minn HCP and other cohorts

Table 1. Connectome Features

Diffusion imaging detects white matter by registering orientation bias of water molecules sequestered within myelinated axons. The majority of dMRI studies focus on differences in specific connections between groups treatment groups. In contrast, we seek here to present a robust, fully populated average connectivity matrix for the entire cortex using data from a large, healthy sample. dMRI fiber tract tracing algorithms can be broadly organized into three classes: local deterministic e.g. dsi-studio (Yeh, Verstynen, Wang, Fernández-Miranda, & Tseng, 2013) or FACT (Mori, Crain, Chacko, & Van Zijl, 1999), local probabilistic e.g. probtrackX (Behrens et al., 2007) or MRtrix (Tournier et al., 2019), and global probabilistic e.g. TRACULA (Yendiki et al., 2011) or (Hagler et al., 2009). Local methods consider the diffusion model at each step when tracing a streamline from a seed region while global methods solve for the most

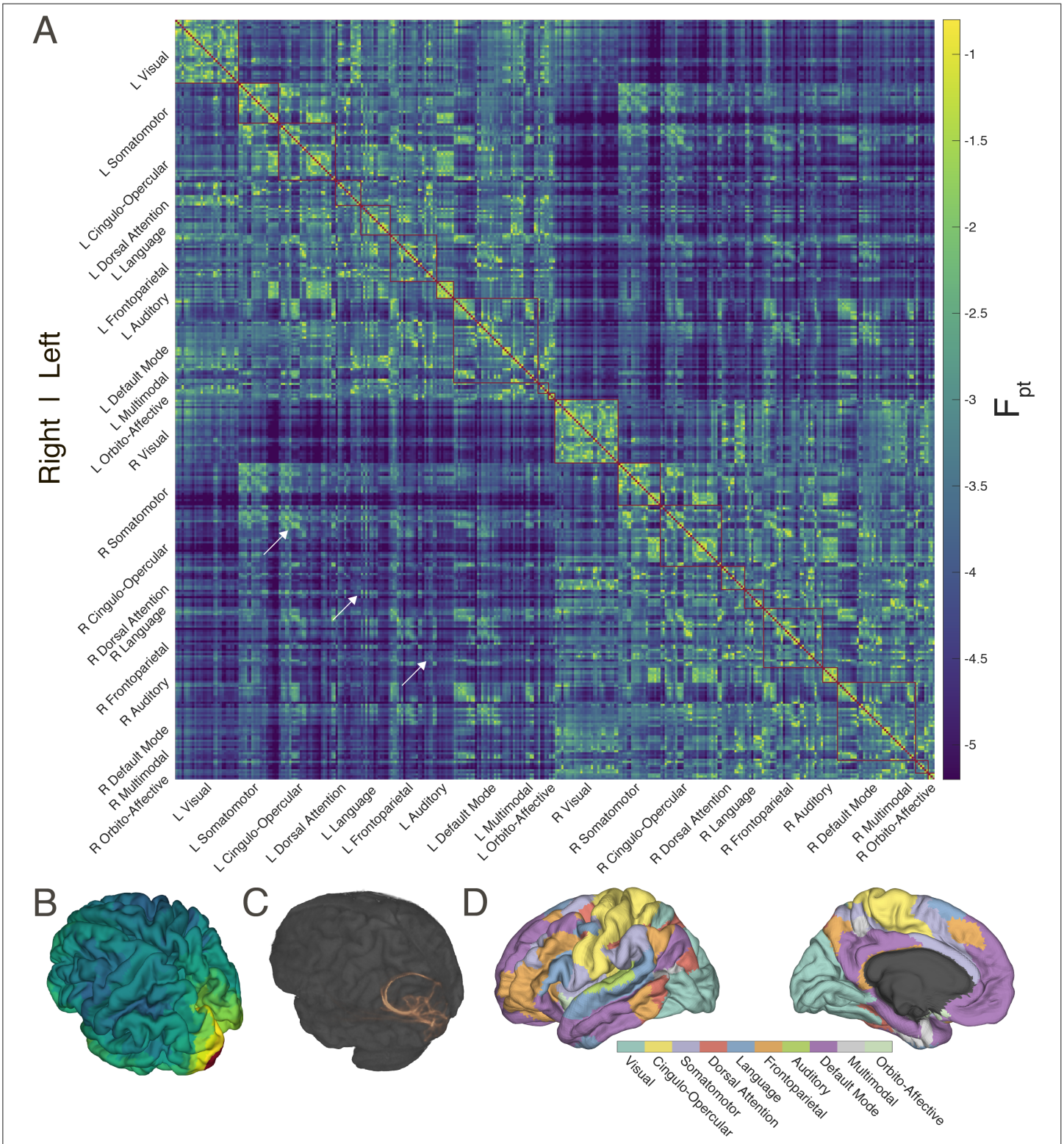

Figure 1. Probabilistic diffusion tractography structural connectome of the human cortex (**A**) Group average (N = 1065) structural connectivity matrix consisting of the 360 HCP-MMPS1.0 atlas parcels organized into ten functional networks. Raw streamline counts are fractionally scaled yielding the log probability F_{pt}. The white arrows highlight the diagonal which contains contralateral homologs. (**B**) The first row of the connectivity matrix, showing connection probabilities from left V1 to all other parcels, projected onto the fsaverage template cortex. (**C**) Single subject (100307) volume ray casting visualization of left V1-originating streamline probabilities within the skull-stripped T1-weighted structural MR volume. (**D**) Ten functional networks, adapted from (Ji et al., 2019), within HCP-MMPS1.0 atlas. These are indicated by red boxes in panel **A**.

likely configuration of the entire volume at once. Deterministic tractography considers only the most likely orientation at each voxel yielding the maximum likelihood tracts whereas probabilistic tractography considers the entire distribution of possible orientations, yielding a probability cloud of connections. Global tractography is best suited to quantifying large, established tracts and deterministic tractography to finding the single most likely route of a streamline. See (Jeurissen, Descoteaux, Mori, & Leemans, 2019) or (Yendiki, 2017) for a review of diffusion tractography methods. As our goal is instead to explore all possible connections between regions, we employed local, probabilistic tractography (Behrens et al., 2007; Jenkinson et al., 2012). This method has been validated against macaque retrograde tracers within-species (Donahue et al., 2016) and the MR scanner and dMRI acquisition protocol used for the WU-Minn HCP database were both optimized in anticipation of this analysis (Sotiropoulos et al., 2013).

When discretizing any connectivity matrix, the choice of node definitions is important. The physiological relevance of the resulting connectome is maximized if nodes form functionally distinct areas and, within the scope of cerebral cortex, this amounts to selecting a cortical parcellation scheme. The HCP multi-modal parcellation (HCP-MMP1.0) (Glasser et al., 2016a) has several advantages: it's boundaries are both functionally and anatomically guided, it has sufficient parcels (360) to generate a rich connectome while few enough that the parcels' extents compare favorably to the dMRI voxel size, and mechanisms exist (Coalson, Van Essen, & Glasser, 2016; Fischl et al., 2004) for it to be readily applied to individuals. Lastly, and most importantly, the HCP-MMP1.0 parcellation is publicly available and widely adopted, facilitating the comparison of the generated matrices to other existing structural and functional connectomes.

Given the computational intensity of dMRI fiber tractography and the field's inclination towards elucidating specific connections, it is not surprising that the number of existing publicly available dMRI datasets exceeds that of finished, readily applicable connectivity matrices. However, there do exist some prior examples. The USC Multimodal connectivity database (http://umcd.humanconnectomeproject.org), (Brown, Rudie, Bandrowski, Van Horn, & Bookheimer, 2012), contains two diffusion imaging tractography connectomes with standard surface-based parcellations: Hagmann (Hagmann et al., 2008) and ICBM (Mori et al., 2008), with sample-sizes of 5 and 138, respectively. A third is available at http://www.dutchconnectomelab.nl which contains 114 controls. All of these use the Desikan-Killiany atlas (Desikan et al., 2006) which consists of 68 cortical parcels and were produced with local, deterministic tractography. The structural connectome presented here has several advantages compared to these. An atlas of major fiber tracts for the HCP 1200 cohort has recently released at http://brain.labsolver.org, (Yeh et al., 2018). However, this deterministic tractography connectome is spatially coarse, consisting of only 54 cortical parcels, and lacks dynamic range, as the connectivity matrix is nearly binary. The HCP-MMP1.0 atlas (Glasser et al., 2016a) has more than five times as many parcels while retaining functional distinctness of areas. Smaller parcels employed are therefore less sensitive to functionally spurious connectivity. In contrast to the relatively sparse existing matrices, the probabilistic tractography (Behrens et al., 2007) approach is sensitive to weak or low probability connections. In fact, our group average connectome is fully connected, i.e. it has a network density of 1.0. Furthermore, the cohort studied (Van Essen et al., 2013) is an order of magnitude larger, and many other types of data are publicly available for the same individuals including the NIH toolbox (Gershon et al., 2013) of neurological and behavioral assays, as well as analyzed fMRI (and for some subjects MEG) data for both quiescent waking and cognitive tasks, permitting within-cohort comparison to functional connectivity.

The following report presents a novel structural connectome of the human neocortex based on probabilistic diffusion tractography. The connectome is partially validated against retrograde tracing in macaques and the relationship between tract length and connection strength is quantified. Further validation is provided by reasonable connectivity properties between contralateral homologous parcels, within language cortex, and between parcels lying at similar levels of the cortical hierarchy.

Network Theory Metrics	
Mean Clustering coef. (MCC)	0.61
Characteristic Path Length (CPL)	1.90
Global Efficiency	0.58
Modularity	0.43
Gamma (normalized MCC)	2.43
Lambda (normalized CPL)	1.07
Small Worldness (Gamma / Lambda)	2.27
Transitivity	0.53
Assortativity	0.03
Raw Density	1.00
Raw Edge Weight, Mean	-3.90
Raw Edge Weight, Std. Dev.	0.81
Thresholded Density	0.20
Thresholded Edge Weight, Mean	-1.34
Thresholded Edge Weight, Std. Dev.	0.27

Table 2. Network theory metrics. Probabilistic diffusion tractography connectome was converted to a binarized graph at a network density of 0.2 before metric calculation.

Results

A whole-cortex structural connectome

Figure 1A shows the group average parcel to parcel and probabilistic diffusion tractography connectome. This matrix consists of connectivity among 360 cortical parcels and is further organized into 10 functional groups (Ji et al., 2019) per hemisphere. The raw probabilistic tractography streamline counts have been normalized by fractionally scaling (Eq. 1) into log probabilities (F_{pt}) following procedures developed for tracing non-human primate connectivity. As dMRI reveals structural connections, the network is undirected and therefore symmetric. The main diagonal is masked as intra-parcel connectivity was not examined in this study. The upper left quadrant shows connectivity among the 180 parcels of the left hemisphere, the lower right quadrant the connectivity within the right hemisphere. The upper right and lower left quadrants are duplicates and show the inter-hemispheric, or callosal, connections. The 180th (or half-) diagonal is clearly visible (white arrows); this shows the connectivity between homologous parcels in the right and left hemispheres, which is greater than non-homologous callosal connectivity for most parcels.

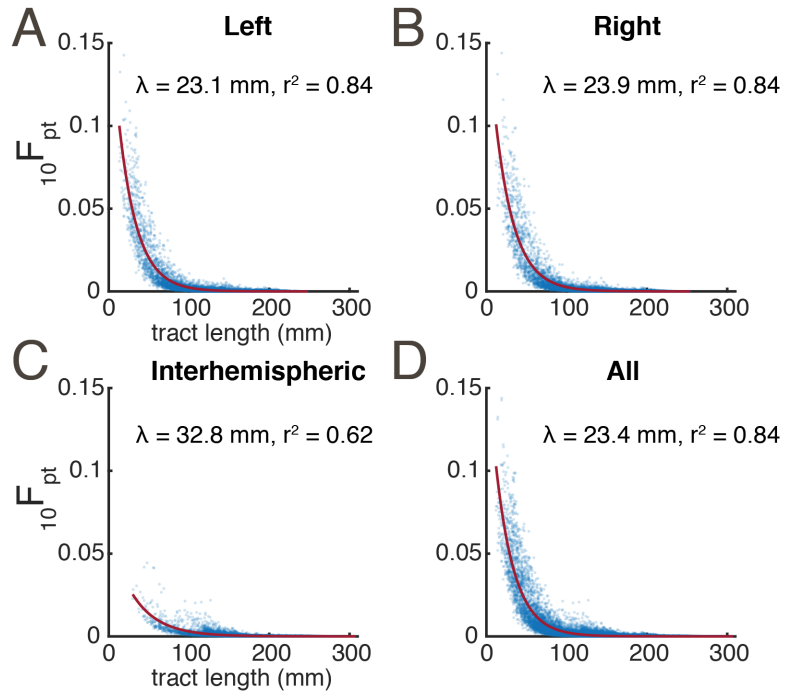

Figure 2. Connectivity strength exponential decays with fiber tract length. (**A**) and (**B**) connections within the right and left hemispheres, respectively. (**C**) Connections between the right and left hemisphere. (**D**) All connections. Each marker represents a pair of parcels. Red traces show the least-squares exponential fit; inset are the length constant λ and r^2 of this fit.

After $\log_{10}$ transformation, F_{pt} connectivity among all parcel pairs is approximately Gaussian in distribution with a mean -3.903 ($CI_{95\%}$ = [-3.910 -3.897]), standard deviation 0.8111 ($CI_{95\%}$ = [0.806 0.816]), skewness 0.627 ($CI_{95\%}$ = [0.6082 0.6440]), and kurtosis 3.605 ($CI_{95\%}$ = [3.5603 3.6498]). In addition to bringing the range of F_{pt} values into the same order of magnitude, $\log_{10}$ transformation is justified as it brings the distribution's skewness significantly closer to zero (pre-$\log_{10}$: 9.047, $CI_{95\%}$ = [8.719 9.469]), and kurtosis significantly closer to three, pre-$\log_{10}$: 103.684 ($CI_{95\%}$ = [93.991 117.026]) thus bringing the distribution closer to normality. See supplementary figure S1 for a graphical comparison. Empirical confidence intervals were estimated via bootstrapping with 2000 iterations.

In the group average connectome, every parcel pair has non-zero connectivity, i.e. a network density of 1. The completeness of the connectivity is due to probabilistic tractography's inclusion of low-probability connections and the statistical power afforded by the large sample size. To further describe the connectome, the network was thresholded to a network density of 0.2 and binarized, and then a variety of network theoretic measures (Rubinov & Sporns, 2010) computed, see table 2 and the supplementary materials. While these values are difficult to interpret in isolation, as expected the thresholded and binarized diffusion connectome is a small world network (small worldness >> 1) ,(Humphries & Gurney, 2008). The ordered full list of parcel labels or nodes can be found in table 3. The values of connectivity matrix, or edge weights of this network can be found in the supplementary files.

Tract length strongly predicts connectivity strength, with exponential decay

In addition to the connection strength, diffusion tractography estimates the fiber tract length between all pairs of parcels. As shown in figure 2, structural connectivity ($10\text{^}F_{pt}$) falls off as an exponential function of fiber tract length with the form $10\text{^}F_{pt} = \alpha * e^{-d/\lambda}$ where λ is the length constant, α the scaling coeffect, and d the tract length. Note that λ is sometimes reported in inverted units of mm^{-1}, e.g. (N. T. Markov et al., 2013; Theodoni et al., 2020), but we here use the λ convention from neuronal cable theory (Dayan & Abbott, 2001) which has more intuitive units (mm); the conventions are conceptually equivalent. For the group-average connectome, λ = 23.4 mm and the least squares

exponential fit explains 84% of the variance in $10^{F_{pt}}$ across all parcel pairs. Callosal connectivity, when isolated, decays more slowly with respect to tract length, $\lambda = 32.8$, and hews to the exponential expectation less consistently $r^2 = 0.62$. Because the tracing of long fiber tracts may be hampered by poor scan quality, we investigated the effects of subjects' motion on λ. For each subject, λ was calculated for non-zero connections in the same manner as the group average. While subjects' motion within the scanner does reduce λ, this effect is modest, only explaining 1.96% of the inter-subject variance, see figure S2.

Probabilistic tract tracing with dMRI reasonably predicts retrograde tracing in macaques

The development of both the HCP-MMP1.0 human cortical atlas (Glasser et al., 2016a) and FV91 macaque parcellation scheme (Felleman & Van Essen, 1991) were led by David Van Essen and the parcel names of these atlases have considerable overlap, particularly for visual and visual association areas. We therefore assumed that parcels with the same name were roughly homologous and limited the scope of the inter-species comparison to these parcels. Furthermore, the macaque FLne values found in (N. T. Markov et al., 2014) are directly comparable to fractionally scaled pt values (Donahue et al., 2016). Comparing the pairwise connectivity between species, we found a Pearson correlation of $r = 0.35$ ($p = 0.0013$), see figure 3. This compares favorably to the $r = 0.59$ found by (Donahue et al., 2016) when comparing retrograde tracing and probabilistic diffusion tractography within the macaque species.

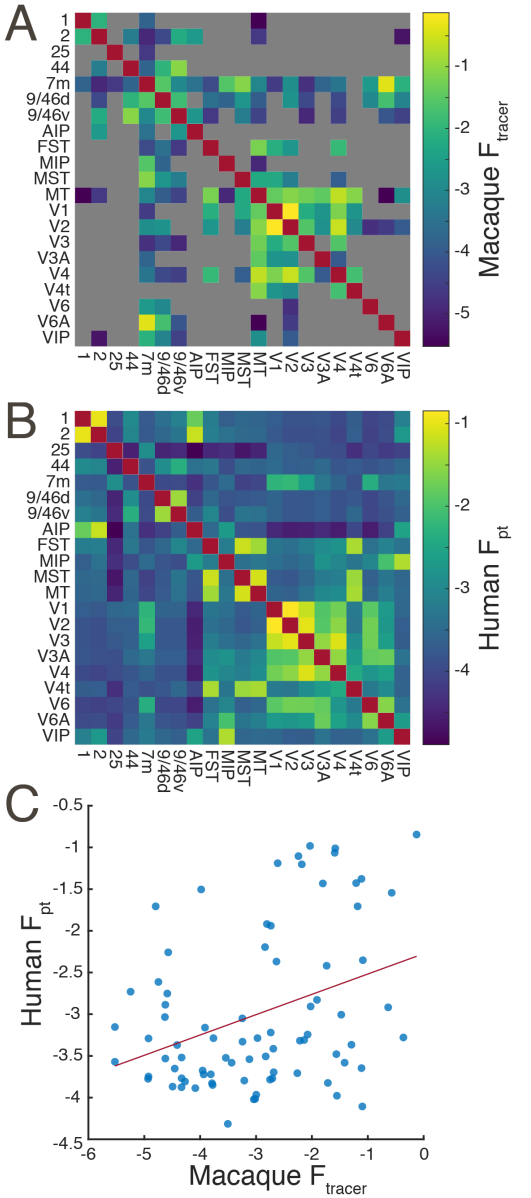

Figure 3. Comparison of human diffusion tractography and macaque retrograde tracing connectomes. Subset of homologous parcels in the human HCP-MMPS1.0 and macaque fv91 atlas. (**A**) Macaque group-average retrograde tracer derived structural connectome, gray indicates missing data. (**B**) Human probabilistic diffusion tractography connectome. (**C**) Pairwise correlation between macaque and human structural connectivity, $r = 0.35$, $p = 0.0013$.

Contra-lateral connectivity is greater in areas underlying unitary processing

On the whole, cortical connectivity is dominated by ipsilateral connections. This effect is readily-observed by comparing the ipsilateral and contralateral quadrants of figure 1A. However, there are exceptions to this rule. The differential connectome of ipsi- vs. contra-lateral connections is shown in figure 4. This is achieved by subtracting the mean of left-right and right-left contralateral connectivity from the mean of the right and left ipsilateral connectivity, i.e. subtracting the mean of the first and third quadrants from the mean of the second and fourth. Areas implicated in motor planning (parcels 5m, 5L, 24dd, and 24dv) are more strongly connected to most contralateral cortex than ipsilateral cortex. Lateromedial connectivity in areas broadly processing space (LIPv, VIP, 7AL, 7PC, 1, 2, 3a, 6d, 31a, 31pd, PCV) and emotion (a10p, a9-46v, a10p, p10p, p47r, p9-46v, 11l, IFSa, IFJp, a24, d32, p32, 10r) is stronger between hemispheres than within them. A possible commonality between these three regions is that space, emotion, and action planning are all unitary percepts. Conversely, the entire auditory network and superior temporal cortices (STGa, STSda, DTDdp, A5, and TPOJ1) as well as the operculum and temporoparietal junction (Ig, MI, FOP1-FOP5, OP1-OP4, PF, PFcm, PFop, PI, PoI1, PoI2, and 43) have hyper-ipsilateral connectivity, consistent with the low transmission latency required for auditory processing, the left-lateralization of language, and the right lateralization of attention.

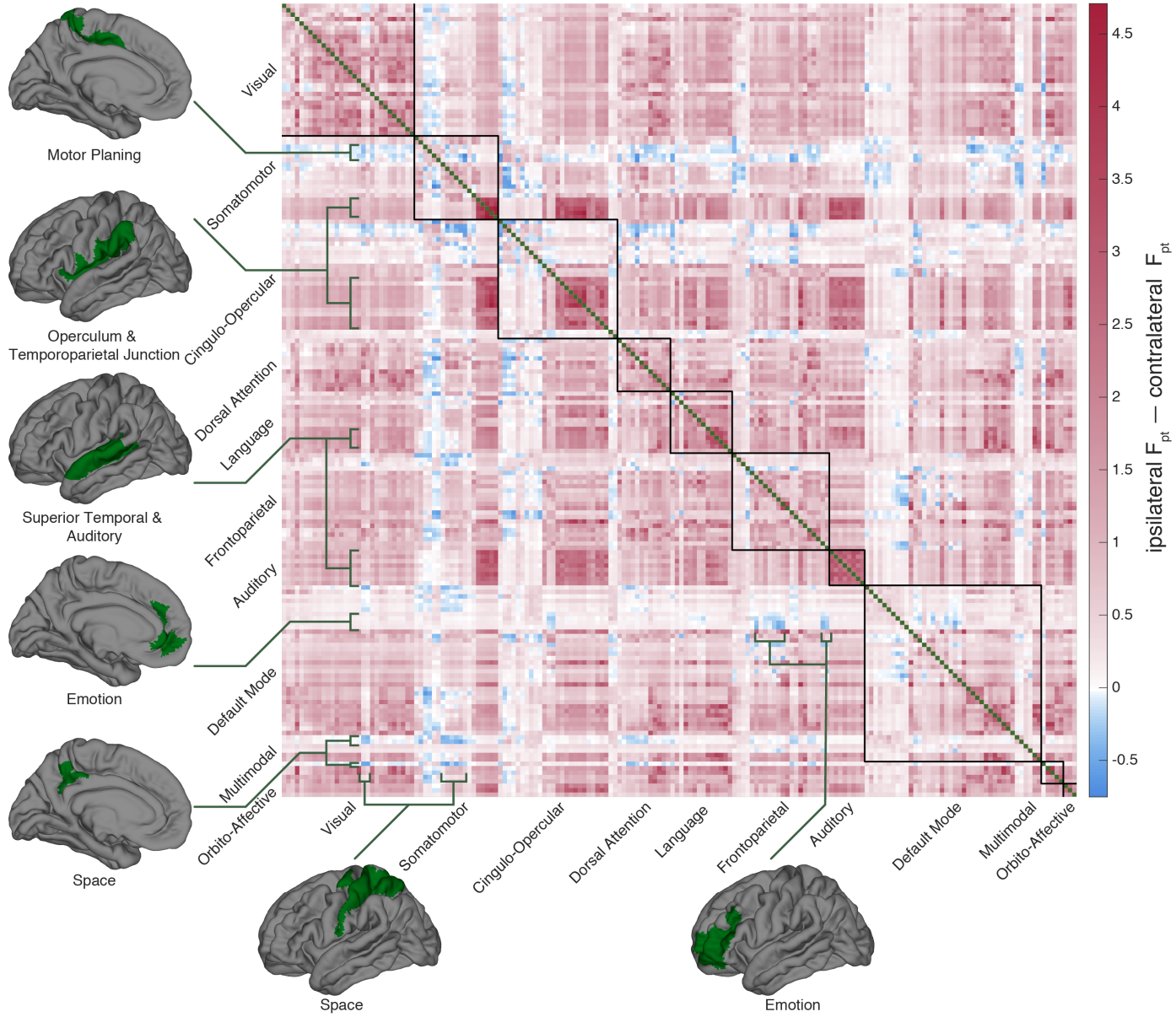

Figure 4. Interhemispheric connectivity. Differential connectivity between ipsilateral and contralateral connectivity. Greater Ipsilateral connectivity dominates and is indicated in red. Parcel-pairs with greater *contra*lateral connectivity than ipsilateral are blue. The anatomic extent of parcel groups of notable contrast are shown on left and bottom of the figure.

Most parcels are disproportionately connected to their contralateral homologs

The two hemispheres of the cortex have a high degree of functional and anatomical symmetry. It follows then that most regions will have greater connectivity to their contralateral homologs than other contralateral areas, in order to coordinate their overlapping processing tasks. This is hinted at by the visibility of the 180th, (or half-) diagonal in figure 1A. To further quantify this effect, for all 180 parcels we compared the connectivity between interhemispheric homologs to the mean of all other callosal connectivity. Bonferroni corrected, empirical 95% confidence intervals were estimated via bootstrapping with 2000 iterations. As detailed in Table S1 and visualized in Figure 5, 147 parcels are hyperconnected to their contralateral homologs, 18 are hypoconnected, and 15 have homologous callosal connectivity not significantly different than their callosal mean connectivity. Interestingly, parcels that are not hyper-connected to their contralateral homologs are concentrated within and adjacent to the language network, consistent with the greater degree of lateralization in these areas.

The language network is hyper-connected at long distances and left lateralized

In order to investigate distance-resolved left laterality in connections among language-implicated cortex, pairwise connections were binned by fiber tract length in 15 mm increments. Within each bin, connections were grouped as being within the combined language and auditory network, or between the combined networks and the rest of the cortex. For each subject, the F_{pt} of grouped connections within each bin was averaged before being log-transformed. The grand-averages of these within- and between- language/auditory cortex in each distance bin for each hemisphere are shown in figure 6A. Bonferroni corrected, empirical 95% confidence intervals for these grand-averages were estimated via bootstrapping with 2000 iterations. Within-language connectivity is slightly attenuated at distances less that 100 mm, but strongly amplified at distances above 100 mm, especially ~100-140 mm connections in the left hemisphere. A plurality of these are between frontal and temporoparietal language areas (18/45 connections between 100 and 140mm). The differential traces of between- vs. within-language connectivity (figure 6B) clearly show the left-hemisphere dominance of this effect.

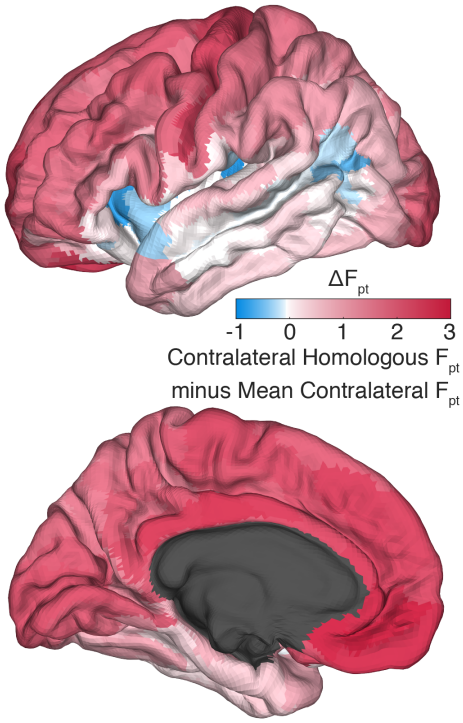

Figure 5. Contralateral homologs. Differential connectivity between contralateral homologous parcels vs the mean of all other contralateral parcels. Red indicates contralateral homologous connectivity greater than mean contralateral connectivity. Note that many language-implicated regions have relatively weak connectivity with their contralateral homologs.

Connectivity is influenced by the cortical hierarchy

Hierarchy is a central organizing principle of the cortex (Burt et al., 2018; Felleman & Van Essen, 1991; Nikola T. Markov et al., 2014; Theodoni et al., 2020). Higher order areas, e.g. supporting abstract processing, have low myelination and lower order areas, e.g. supporting unimodal sensory processing, have high myelination. Furthermore, areal myelination is indexed by the ratio between T1- and T2-wieghted MRI contrast (Glasser & Van Essen, 2011). The WU-Minn HCP 1200 release includes smoothed group-average myelination indices for all vertices in the 32k grayordinate template brain. These values were averaged for each parcel in the HCP-MMP1.0 atlas (Glasser et al., 2016a) to yield a group-average parcel-wise index of myelination.

The relationship between cortical hierarchy and connectivity was assessed in two ways. We first examined whether regions of similar level in the cortical hierarchy are better connected, as predicted by (Barbas, 2015). An index of hierarchical similarity, $F_{|\Delta\ myelination|}$, was obtained for each pair of parcels by computing the pairwise difference in myelination between parcels and fractionally scaling it in the same manner as F_{pt}, with smaller values indicating hierarchical closeness. The similarity matrix created by this derivation is shown in figure S3. Correlations were obtained for the left and right hemisphere as a whole as well as the colossal connections, figure 7A. In addition, for each of the twenty functional networks (10 per hemisphere) the Pearson correlation between the $F_{|\Delta\ myelination|}$ and F_{pt} for pairwise within-network connections was computed, see figure 7B. With the exception of the interhemispheric connections, calculations were performed on the hemispheres separately to avoid the collinearity introduced by hemispheric homology.

With the exceptions of the bilateral visual and somatomotor networks and right language network, for which there is convincingly no relationship, the preponderance of coefficients are negative, indicating that, on average, areas at similar levels of the cortical hierarchy are better connected. However, quantified in this way, the influence of hierarchy is modest, explaining about 1% of the variance in F_{pt} overall, though perhaps 10-30% in certain subsets of parcels, such as the left auditory and language networks. The left lateralization of the influence of hierarchy in these networks is striking, as is the right-lateralization of the dorsal attention network.

Secondly, we investigated whether a cortical region's hierarchical level affected its overall connectivity. For each parcel, the Pearson correlation between the parcel's F_{pt} to all other parcels and the parcel-wise index of myelination was computed. In other words, correlation between each row of the connectome matrix and the vector of myelination indices was obtained. After Bonferroni correction for multiple comparisons, 74 of 360 parcels (see tables S2, S3) have

connectivity significantly correlated to their myelination index and of these the vast majority (70) are negatively correlated, indicating that low myelination predicts high connectivity, see figure 7C. These areas form a contiguous bilateral prefrontal network as shown in figure 7D, indicating that prefrontal areas are more connected with higher cortical regions. The rare positively correlated exceptions are the left and right DVT and V6A.

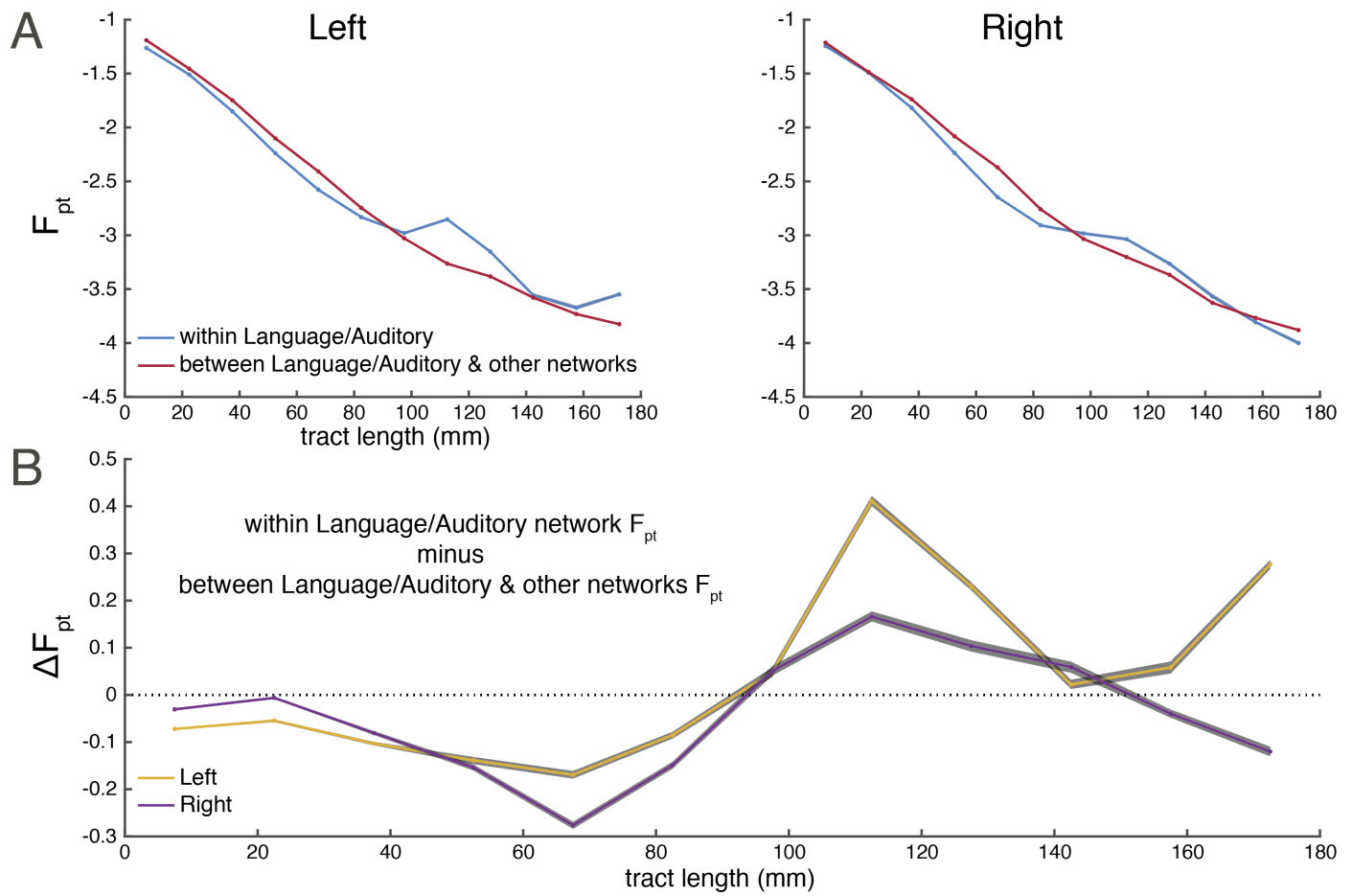

Figure 6. Language/Auditory network hyperconnectivity and left-lateralization. (**A**) Distance-binned connectivity within the language and auditory networks compared to connectivity between the language and auditory networks and other networks, separately for the left and right hemispheres (**B**) The differential trace for the within- and between- connectivity in both hemispheres. In both panels, gray patches show Bonferroni-corrected bootstrapped 95% confidence intervals across subjects.

Discussion

In this study we compiled a whole-cortex structural connectome by applying probabilistic tractography to the diffusion MR volumes of 1065 subjects from the WU-Minn Human Connectome Project. We report a novel, complete, and high-dynamic-range connectivity matrix discretized into the 360 parcels of the HCP-MMP1.0 atlas and further arranged into 10 functional networks. It is shown that connectivity strength exponentially decays with fiber tract length, that the parts of the connectome with clear homology to macaques correspond reasonably to retrograde tracer mappings in that species, that contralateral homologs are hyperconnected, and that connections within language-implicated cortex are left-lateralized. Analysis suggests that cortical areas underlying unitary processing have relatively high colossal connectivity. Cortical areas tend to be more connected with areas at similar levels of the cortical hierarchy, as indexed by their estimated myelination, particularly in prefrontal areas. In sum, we quantify a dMRI-based estimate of medium- to long-range anatomical cortico-cortical connectivity in a large normative sample.

Diffusion MR imaging and automated post-hoc tractography are powerful tools for the elucidation of cerebral connectivity. The defining advantages of these techniques are non-invasiveness and large field-of-view, enabling whole-brain mapping in humans. However, dMRI does have significant limitations when compared to

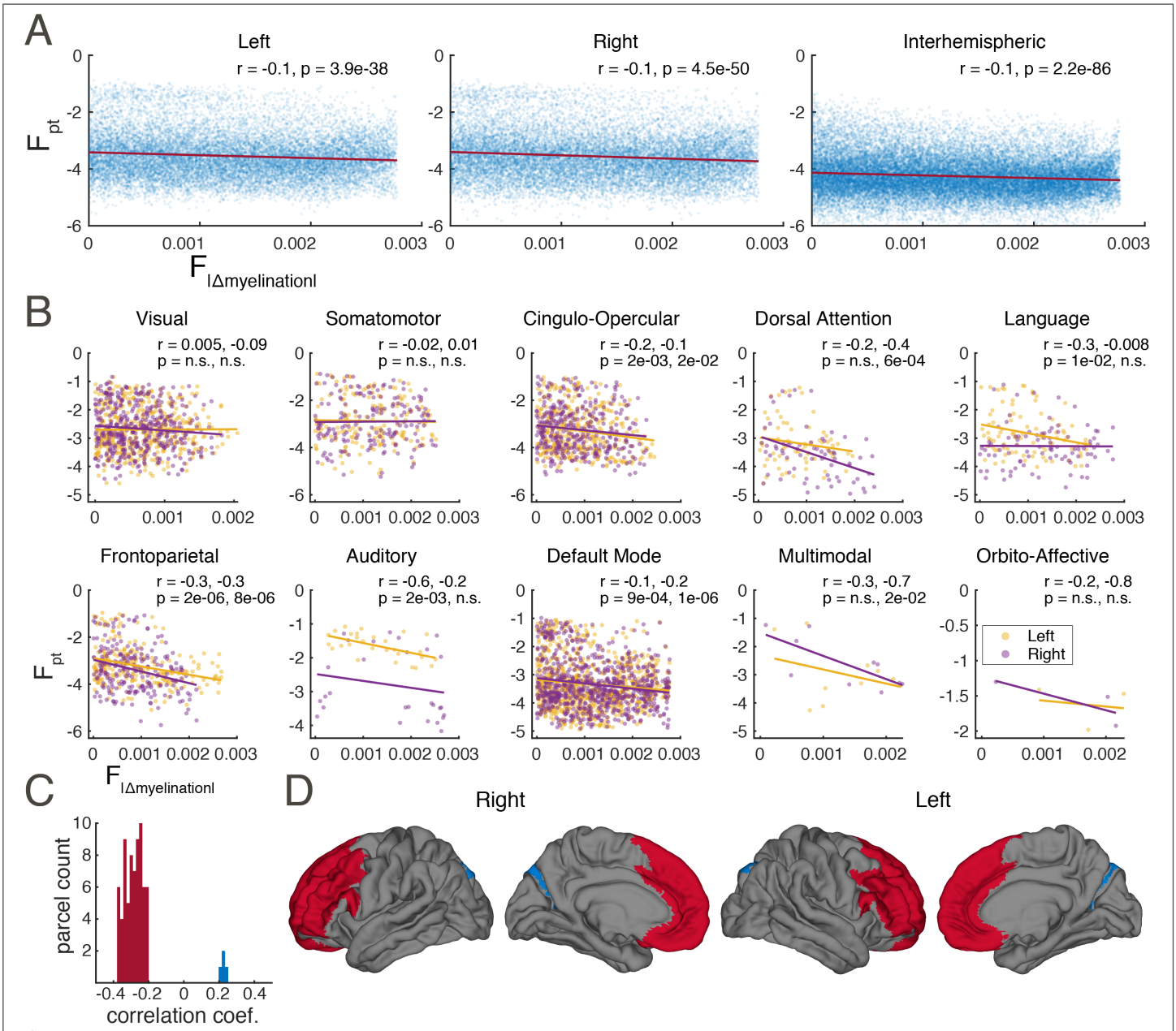

Figure 7. Connectivity is influenced by the cortical hierarchy. (**A**, **B**) Connectivity is strongly predicted by hierarchical similarity in some networks and modestly predicted overall. (**A**) All connectivity vs. myelination difference, including within- and across-network connections, for the left, right, and callosal connections. For both panels, each marker represents a parcel pair. (**B**) Within-network connectivity vs. myelination difference for 10 functional networks. Linear fits and correlation coefficients computed independently for the left and right hemisphere. A negative correlation indicates that parcels at similar hierarchical levels tend to be more connected. (**C**, **D**) Higher order prefrontal areas are better connected. (**C**) Histogram of correlation coefficients between areal myelination and F_{pt} connectivity to each parcel. Only significant coefficients after Bonferroni correction are shown. Most coefficients are negative indicating high connectivity to low-myelination (i.e., higher-order) areas. (**D**) Significant negative coefficients (red) map onto bilateral prefrontal cortex. Only the bilateral DVT and V6A are show positive significant correlations (blue).

immunohistology, EM microscopy, or stimulation. The most obvious of these is insensitivity to whether underlying axons are anterograde or retrograde, as evidenced by the symmetry of the connectivity matrix. The anisotropic diffusion of water molecules occurs in both anterograde and retrograde directions. Thus, the true one-way connectivity between two areas could be anywhere between none to all of the symmetric diffusion connectivity. Another important limitation is spatial resolution. While the 1.25 mm isotropic voxels achieved by the WU-Minn dMRI protocol are smaller than those of most studies (Jeurissen et al., 2019), they are still more than three orders-of-

magnitude larger than the typical submicron axon diameter (Liewald, Miller, Logothetis, Wagner, & Schüz, 2014; von Keyserlingk Graf & Schramm, 1984). This discrepancy is particularly impactful when fiber orientations are not consistent within a voxel, i.e. crossing fibers. Probabilistic diffusion tractography (Behrens et al., 2007) partially ameliorates the issue by modeling the probability distribution of orientations and accounting for uncertainty, but ultimately dMRI with current technology is a meso- to macroscale technique. Direct histological validation of dMRI techniques is uncommon, but has been performed in non-human primates for the probabilistic diffusion tractography pipeline used in this study (Donahue et al., 2016).

When constructing this connectome, we divided the cortex into 180 parcels per hemisphere following the HCP-MMP1.0 atlas (Glasser et al., 2016b). To ease interpretation, we further organized the parcels into 10 functional networks modified from (Ji et al., 2019). These networks were created by applying iterative Louvain clustering (Blondel, Guillaume, Lambiotte, & Lefebvre, 2008; Rubinov & Sporns, 2010) and other criteria to HCP resting state fMRI data. While these fMRI-defined network definitions correspond reasonably to the structural connections reported here, there are exceptions. The operculum and temporoparietal junction, in particular, appears to be a structurally distinct area that has been folded into several functional networks (Ji et al., 2019). However, this contiguous region forms the lateral salience network in (Barnett et al., 2020) which similarly applied a very similar methodology to a non-HCP cohort. Like many cortically-focused studies, we used a surface-based methodology to define these areas, with seed and target regions constrained to the white-matter – gray-matter interface. This approach reduces the overrepresentation of major bundles (Jeurissen et al., 2019), enables the automated assessment based on inter-subject homology (Fischl, Sereno, Tootell, & Dale, 1999), facilitates comparison to other cortical datasets, and is true to the anatomical nature of the cortical ribbon. Unfortunately, the subcortex and cerebellum are omitted in this analysis, as are short-range, often unmyelinated, intra-parcel connections. The inclusion of the thalamic radiations, in particular, is a merited future extension of this connectome.

The atlas used was selected because of its wide adoption, symmetry, and high parcel count. Furthermore, the parcels are based on multiple functional and anatomical criteria and are consistent with previous functional parcellations in human and non-human primates (Felleman & Van Essen, 1991; Glasser et al., 2016b). Because the parcels are relatively small and informed by function, erroneous averaging of disparate connections, a connectomic extension of the partial volume artifact, is minimized. However, this comes at the cost of non-uniformity in both parcel area and shape. Methodologically, parcels are assembled from vertices on the tessellated cortical surface. A future vertex-based connectome, while computationally challenging, would have the distinct advantage of being readily reformulated into any arbitrary surface-based parcellation scheme.

We found that pairwise connectivity between cortical parcels exhibits an exponential decay rule with respect to fiber tract distance with a length constant λ of ~23 mm (~33 mm for callosal connections). Histological studies in non-human primates (Donahue et al., 2016; N. T. Markov et al., 2013; Theodoni et al., 2020) consistently show exponential connectivity decay with distance. Such a rule when combined with a roughly Gaussian distribution of interareal distances explains the observed log-normal distribution of connectivity strength (N. T. Markov et al., 2013). Histological data indicate a λ of about 3.33 mm for marmosets (Theodoni et al., 2020) and 5.55 mm for macaques (N. T. Markov et al., 2013). Across species, there appears to be a linear relationship between the logs of λ and total gray matter volume, predicting a human λ of 10 mm (Theodoni et al., 2020). While methodological differences between diffusion and histological tractography cannot be completely ruled out, Donahue and colleagues found similar λ for the two methods in macaques (Donahue et al., 2016). Our results suggest that, compared to other species, human cortical areas are exceptionally well connected relative to their cortical volume, reflected in a disproportionately long λ.

Geometric scaling strongly constrains cortico-cortical connectivity in humans. Considering primate brains increasing in diameter d, volume and number of cortical neurons increases by d^3,(Ventura-Antunes, Mota, & Herculano-Houzel, 2013), so arriving at a constant probability of connection between any two neurons would require d^6 axons, and since they would need to be about d times as long, this would require a volume proportional to d^7, or more if axonal diameter is increased to maintain a relatively constant latency of communication (Wang et al., 2008). However, the actual white matter volume is less than d^4 (Zhang & Sejnowski, 2000), and consequently the probability of cortico-cortical connectivity must be highly limited in humans. The relatively long λ in humans we report reduces even further the number of connections which can be accommodated within the available white matter volume. A consequence of fewer but longer connections would be reduced metabolic cost, inasmuch the cost of an action potential is 1/3 axonal transmission (proportional to length) and 2/3 synaptic transmission (Lennie, 2003). The low

Idx.	Parcel	Orig.	Network	Idx.	Parcel	Orig.	Network	Idx.	Parcel	Orig.	Network
1	V1	1	Cingulo-Opercular	**61**	46	84	Cingulo-Opercular	**121**	IP1	145	Frontoparietal
2	ProS	121	Visual	**62**	9-46d	86	Cingulo-Opercular	**122**	PFm	149	Frontoparietal
3	DVT	142	Visual	**63**	43	99	Cingulo-Opercular	**123**	p10p	170	Frontoparietal
4	MST	2	Visual	**64**	PFcm	105	Cingulo-Opercular	**124**	p47r	171	Frontoparietal
5	V6	3	Visual	**65**	PoI2	106	Cingulo-Opercular	**125**	A1	24	Auditory
6	V2	4	Visual	**66**	FOP4	108	Cingulo-Opercular	**126**	52	103	Auditory
7	V3	5	Visual	**67**	MI	109	Cingulo-Opercular	**127**	RI	104	Auditory
8	V4	6	Visual	**68**	FOP1	113	Cingulo-Opercular	**128**	TA2	107	Auditory
9	V8	7	Visual	**69**	FOP3	114	Cingulo-Opercular	**129**	PBelt	124	Auditory
10	V3A	13	Visual	**70**	PFop	147	Cingulo-Opercular	**130**	MBelt	173	Auditory
11	V7	16	Visual	**71**	PF	148	Cingulo-Opercular	**131**	LBelt	174	Auditory
12	IPS1	17	Visual	**72**	PoI1	167	Cingulo-Opercular	**132**	A4	175	Auditory
13	FFC	18	Visual	**73**	FOP5	169	Cingulo-Opercular	**133**	7m	30	Default Mode
14	V3B	19	Visual	**74**	PI	178	Cingulo-Opercular	**134**	POS1	31	Default Mode
15	LO1	20	Visual	**75**	a32pr	179	Cingulo-Opercular	**135**	23d	32	Default Mode
16	LO2	21	Visual	**76**	p24	180	Cingulo-Opercular	**136**	v23ab	33	Default Mode
17	PIT	22	Visual	**77**	PEF	11	Dorsal Attention	**137**	d23ab	34	Default Mode
18	MT	23	Visual	**78**	7PL	46	Dorsal Attention	**138**	31pv	35	Default Mode
19	LIPv	48	Visual	**79**	MIP	50	Dorsal Attention	**139**	a24	61	Default Mode
20	VIP	49	Visual	**80**	LIPd	95	Dorsal Attention	**140**	d32	62	Default Mode
21	PH	138	Visual	**81**	6a	96	Dorsal Attention	**141**	p32	64	Default Mode
22	V6A	152	Visual	**82**	PFt	116	Dorsal Attention	**142**	10r	65	Default Mode
23	VMV1	153	Visual	**83**	AIP	117	Dorsal Attention	**143**	47m	66	Default Mode
24	VMV3	154	Visual	**84**	PHA3	127	Dorsal Attention	**144**	8Av	67	Default Mode
25	V4t	156	Visual	**85**	TE2p	136	Dorsal Attention	**145**	8Ad	68	Default Mode
26	FST	157	Visual	**86**	PHT	137	Dorsal Attention	**146**	9m	69	Default Mode
27	V3CD	158	Visual	**87**	PGp	143	Dorsal Attention	**147**	8BL	70	Default Mode
28	LO3	159	Visual	**88**	IP0	146	Dorsal Attention	**148**	9p	71	Default Mode
29	VMV2	160	Visual	**89**	55b	12	Language	**149**	10d	72	Default Mode
30	VVC	163	Visual	**90**	PSL	25	Language	**150**	47l	76	Default Mode
31	4	8	Somatomotor	**91**	SFL	26	Language	**151**	9a	87	Default Mode
32	3b	9	Somatomotor	**92**	STV	28	Language	**152**	10v	88	Default Mode
33	5m	36	Somatomotor	**93**	44	74	Language	**153**	10pp	90	Default Mode
34	5L	39	Somatomotor	**94**	45	75	Language	**154**	OFC	93	Default Mode
35	24dd	40	Somatomotor	**95**	IFJa	79	Language	**155**	47s	94	Default Mode
36	24dv	41	Somatomotor	**96**	IFSp	81	Language	**156**	EC	118	Default Mode
37	7AL	42	Somatomotor	**97**	STGa	123	Language	**157**	PreS	119	Default Mode
38	7PC	47	Somatomotor	**98**	A5	125	Language	**158**	H	120	Default Mode
39	1	51	Somatomotor	**99**	STSda	128	Language	**159**	PHA1	126	Default Mode
40	2	52	Somatomotor	**100**	STSdp	129	Language	**160**	STSvp	130	Default Mode
41	3a	53	Somatomotor	**101**	TPOJ1	139	Language	**161**	TGd	131	Default Mode
42	6d	54	Somatomotor	**102**	TGv	172	Language	**162**	TE1a	132	Default Mode
43	6mp	55	Somatomotor	**103**	RSC	14	Frontoparietal	**163**	TE2a	134	Default Mode
44	6v	56	Somatomotor	**104**	POS2	15	Frontoparietal	**164**	PGi	150	Default Mode
45	OP4	100	Somatomotor	**105**	7Pm	29	Frontoparietal	**165**	PGs	151	Default Mode
46	OP1	101	Somatomotor	**106**	8BM	63	Frontoparietal	**166**	PHA2	155	Default Mode
47	OP2-3	102	Somatomotor	**107**	8C	73	Frontoparietal	**167**	31pd	161	Default Mode
48	FOP2	115	Somatomotor	**108**	a47r	77	Frontoparietal	**168**	31a	162	Default Mode
49	Ig	168	Somatomotor	**109**	IFJp	80	Frontoparietal	**169**	25	164	Default Mode
50	FEF	10	Cingulo-Opercular	**110**	IFSa	82	Frontoparietal	**170**	s32	165	Default Mode
51	5mv	37	Cingulo-Opercular	**111**	p9-46v	83	Frontoparietal	**171**	STSva	176	Default Mode
52	23c	38	Cingulo-Opercular	**112**	a9-46v	85	Frontoparietal	**172**	TE1m	177	Default Mode
53	SCEF	43	Cingulo-Opercular	**113**	a10p	89	Frontoparietal	**173**	PCV	27	Multimodal
54	6ma	44	Cingulo-Opercular	**114**	11l	91	Frontoparietal	**174**	TPOJ2	140	Multimodal
55	7Am	45	Cingulo-Opercular	**115**	13l	92	Frontoparietal	**175**	TPOJ3	141	Multimodal
56	p24pr	57	Cingulo-Opercular	**116**	i6-8	97	Frontoparietal	**176**	PeEc	122	Multimodal
57	33pr	58	Cingulo-Opercular	**117**	s6-8	98	Frontoparietal	**177**	TF	135	Multimodal
58	a24pr	59	Cingulo-Opercular	**118**	AVI	111	Frontoparietal	**178**	Pir	110	Orbito-Affective
59	p32pr	60	Cingulo-Opercular	**119**	TE1p	133	Frontoparietal	**179**	AAIC	112	Orbito-Affective
60	6r	78	Cingulo-Opercular	**120**	IP2	144	Frontoparietal	**180**	pOFC	166	Orbito-Affective

Table 3. Parcel order and network assignment. The emboldened indices refer to the parcel order in figure 1A. The Orig. indices refer to the original parcel order presented in (Glasser et al., 2016a). All indices refer to the left hemisphere, adding 180 yields the homologous right hemisphere indices.

firing rate of human pyramidal cells (Chan et al., 2014) would also reduce the metabolic cost of their axons. These observations are consistent with the proposal that the metabolic costs of cortico-cortical connections may help constrain their organization in the primate brain (Ercsey-Ravasz et al., 2013). Given this strong correlation of connection strength with distance, as well as the bias of tract-tracing techniques toward shorter, less geometrically complex connections (Jeurissen et al., 2019), there may be some merit in regressing out the effect of tract length when evaluating the relative connectivity of different cortical areas. However, the considerations enumerated above imply a strong evolutionary selection to place cortical parcels which require high connectivity to perform their calculations to be situated in direct physical proximity to each other. The patterns of relatively long distance connectivity identified here thus must be viewed as minor deviations from an overall strong tendency favoring local connectivity, a conceptualization consistent with the view of the cortex as a spatially embedded small world network.

One striking deviation from the distance-based connectivity was the left-lateralized hyper-connectivity between language areas, and specifically between posterior and anterior language areas. This connectivity presumably passes, completely or in part, through the classical language pathways (reviewed in (Dick & Tremblay, 2012)). The lateralization we observed may then reflect that of the arcuate and inferior longitudinal fasciculi which connect the same structures and show significant left lateralization in humans but not macaques (Eichert et al., 2019; Panesar, Yeh, Jacquesson, Hula, & Fernandez-Miranda, 2018). Left-lateralization of the arcuate fasciculus develops late (Lebel & Beaulieu, 2011), and is sensitive to the presence, quality and quantity of early language experience (Cheng, Roth, Halgren, & Mayberry, 2019; Romeo et al., 2018). More generally, many of the connectivity patterns observed here could be the indirect result of co-activation of the connected parcels (Mount & Monje, 2017). The left-lateralized ipsilateral connectivity may be compensated by a relative lack of callosal connections from the same areas, under the hypothesis that the total connectivity is constrained.

A more general factor that might induce deviations from a distance-based connectivity rule may be the principle of hierarchical organization. It has been proposed that distant areas with similar laminar properties, and thus of similar hierarchical order may have privileged connections (Barbas, 2015). Across the entire cortex we find that myelination similarity explains a significant but small amount of the overall variance. However, there are regions where the influence of hierarchical position is more pronounced including the right dorsal attention and left auditory/language networks. The observed hyperconnectivity and high degree of lateralization in these regions may be a consequence of the low-latencies necessary for the functions they underly. More broadly, the effects of transmission latency constraints on neuroanatomy and conduction delay on large-scale physiological recordings are an emerging area of study in human neuroscience (Muller, Chavane, Reynolds, & Sejnowski, 2018). Latency is a hybrid structural–functional property of connectivity, and could be defined using cortico-cortical evoked potentials (CCEP) (Trebaul et al., 2018).

By emphasizing the cortical connectivity matrix over the white matter bundles *per se* and organizing the matrix into the widely adopted HCP-MMP1.0 atlas (Glasser et al., 2016b), the structural connectome reported here enables ready comparison to other structural, functional, and hybrid connectomes. These include source-localized resting-state magneto-encephalography (MEG) (Larson-Prior et al., 2013) and fMRI datasets for subsets of the same HCP cohort (Ji et al., 2019; Van Essen et al., 2013). Neuropsychological metrics, including the NIH toolbox (Gershon et al., 2013) and genotypic data (dbGaP phs001364.v1.p1) are also available for this cohort, enabling future studies of the interplay between cortical connectivity, cognition, and genetics. Although resting-state functional connectivity is constrained by anatomical networks and can be partially predicted by them (Honey et al., 2009), indirect connections or parallel processing of stimuli in different areas can produce correlated activity even in the absence of direct anatomical connections. One example of the latter may be inter-hemispheric homologs. While we did find hyperconnectivity between inter-hemispheric homologs when compared to other callosal connections, anatomical interhemispheric connectivity on the whole is weaker than resting-state fMRI studies have reported (Brown et al., 2012; Ji et al., 2019; Van Essen et al., 2013). The Functional Brain Tractography project (F-TRACT), https://f-tract.eu (Trebaul et al., 2018), has released several CCEP connectivity matrices in the HCP-MMP1.0 atlas. While CCEP connectivity mapping is necessarily incomplete, due to the sparse spatial sampling of human intracranial recordings, they may nonetheless form a bridge between anatomical and physiological understandings of cortical connectivity.

The Human Connectome Project was a scientific undertaking of visionary scope and ambition. It's commitment to open science and accessibility of data by the public enabled this study and will continue to enable further studies for years to come. Emerging clinal applications of brain connectomics will be underpinned by a strong base of normative data for comparison. The whole-cortex probabilistic diffusion tractography connectome reported here fulfills a key

goal outlined in the project's conception and we hope it will empower yet further study of the myriad and beautiful web of connectivity that the human brain embodies.

Methods

Subjects & data sources

No new data was collected for this study, and the existing data used was gathered from publicly available databases. Individual subject's high-resolution T1-weighted structural magnetic resonance volumes (MRI), Diffusion images (dMRI), and source-localized resting-state magnetoencephalography (MEG) data were gathered from the Human Connectome Project's (HCP) WU-Minn 1200 release (Van Essen et al., 2013) at https://db.humanconnectome.org. The diffusion imaging dataset consists of 1065 individuals (575 women), aged 22-36+ years old. These datasets include some twin and non-twin siblings. However, individuals' family structure, as well as exact age, handedness, and ethnicity are access-restricted to protect the privacy of the subjects and these data were not requested as they are not critical to this study. Group-average dense T1w/T2w myelination index were gathered from the same source. Macaque retrograde tracer connectivity was sourced from supplementary table 6 of (N. T. Markov et al., 2014). Parcel-by-parcel values were averaged across monkey and hemisphere.

Cortical parcellation & functional networks

The HCP multimodal parcellation scheme (HCP-MMP1.0), consisting of 180 cortical parcels per hemisphere, was projected from the Workbench (Marcus et al., 2011) 32k grayordinate template brain to the FreeSurfer (Fischl, 2012) ico5 fsaverage template as per (Coalson et al., 2016). Using the FreeSurfer reconstruction directories gathered from the database, surface-based fsaverage parcel labels were mapped onto each individual's white matter surface using spherical landmark registration (`fs_label2label`) ,(Fischl et al., 1999). Finally, individual's surface-based parcel labels were converted to binary volumes marking the gray matter – white matter boundary (`mri_label2vol`) to serve as seed and target regions for probabilistic tractography. Workbench and FreeSurfer functions were sourced from releases 1.2.3 and 6.0, respectively.

In order to facilitate interpretation of the connectome, parcels were ordered and grouped into functional networks adapted from (Ji et al., 2019), which applied iterative Louvain clustering (Blondel et al., 2008; Rubinov & Sporns, 2010) and other criteria to a resting state fMRI connectivity. These functional groupings and parcel order were selected as they were also generated using (a subset of) the WU-Minn HCP dataset and the HCP-MMP1.0 parcellation scheme. For this study the parcels of the left and right hemispheres were separated and the order and groupings of the left hemisphere in (Ji et al., 2019) were used for homologous parcels in the both right and left hemisphere, respectively. Two pairs of the original networks (primary and secondary visual, ventral and posterior multimodal) contained too few parcels for effective analysis and were highly inter-related. These network pairs were simplified by combining them into visual and multimodal groups, yielding 10 functional networks per hemisphere, see table 3.

Probabilistic tractography

All analysis of diffusion imaging data was performed with FSL (Behrens et al., 2007; Jenkinson et al., 2012) release 6.0.1. Analyses were performed identically for each subject and broadly follow (Burns, 2014). The diffusion and bedpostX precursor directories made available from the HCP database were used as inputs without modification.

First, fractional anisotropy (FA) analysis was performed using `dtifit`. The resulting FA volumes were not analyzed but only used for registering the FreeSurfer and dMRI volumes (`flirt`), as is necessary to map the parcel masks into dMRI space (`probtrackx2` arguments `--xfm --seedref`) .

Non-invasive probabilistic tractography was performed with `probtrackx2` in voxel-by-parcel mode (`--os2t --s2tastext`). In this configuration, the number and length of streamlines (`--ompl --opd`) is estimated from each voxel in the seed parcel to each target parcel as a whole. To aid parallelization of these computationally intensive processes, the list of target parcels (`--targetmasks`) was quartered into four sub-lists. Therefore `probtrackx2` was invoked 1440 times per subject, estimating the connectivity between 1 seed parcel and 90 target parcels in each invocation. The default ½ voxel step length, 5000 samples and 2000 steps were used (`--steplength 0.5 -P 5000 -S 2000`). To avoid artifactual loops, streamlines that loop back on themselves were discarded (`-l`) and tractography was constrained by a 90° threshold (`-c 0`) for maximal curvature between successive steps. Within-parcel connectivity and cotico-subcortical

connectivity were not examined in this study. All post-hoc analyses and visualization of connectivity data were performed in Matlab 2019b (Mathworks) except for Fig. 1C which was rendered in `fsleyes`.

Normalization & symmetrization

Raw streamline counts were averaged across all subjects, then normalized and symmetrized following procedure developed for non-human primate histological tracing (Donahue et al., 2016; Theodoni et al., 2020). Briefly, fractionally scaled values are defined as the ratio of the number of streamlines originating at parcel A and terminating at parcel B to the total number of streamlines that either originate at parcel A or terminate at parcel B while excluding within-parcel connections.

Eq. 1 $F(DTI_{i,j}) = \frac{DTI_{i,j}}{\sum_{x=1}^{N} DTI_{i,x} + \sum_{y=1}^{N} DTI_{y,j}}, where\ x \neq i\ \&\ y \neq j$

While diffusion tractography is not sensitive to the directionality of connections, because parcel A to B and parcel B to A streamlines are computed separately minor asymmetries arise. Connectivity matrix symmetry is enforced by taking the arithmetic mean of the A-B and B-A fractionally scaled connection weights.

Eq. 2 $F_{i,j} = \frac{F_{i,j} + F_{j,i}}{2}$

Because probabilistic tractography values span several orders of magnitude, and are approximately log-normally distributed (Fig. S1), data were log-transformed ($\log_{10}$) prior to subsequent analyses.

Data availability

Individual and group average connectivity matrices as well as figure source data other supplementary files are available to download at https://doi.org/10.5281/zenodo.3928848. The preprocessed HCP data using in this study was retrieved from https://db.humanconnectome.org and the preprocessing code used to create these files is availed at https://github.com/Washington-University/HCPpipelines. The source code for FSL, including probtrackx2 is available from https://fsl.fmrib.ox.ac.uk/fsl/fslwiki/FSL. Network theory measures were computed with the brain connectivity Matlab toolbox whose source code is available from http://www.brain-connectivity-toolbox.net.

Acknowledgements

This work was supported by NIMH 1RF1MH117155-01 and 5T32MH020002-19, NINDS 1R01NS109553-01A1, and ONR 00014-16-1-2415. Data were provided, in part, by the Human Connectome Project, WU-Minn Consortium (Principal Investigators: David Van Essen and Kamil Ugurbil; 1U54MH091657) funded by the 16 NIH Institutes and Centers that support the NIH Blueprint for Neuroscience Research; and by the McDonnell Center for Systems Neuroscience at Washington University. We are grateful to Adam Niese and the San Diego Supercomputer Center for providing technical support.

References

Andersson, J. L. R., & Sotiropoulos, S. N. (2016). An integrated approach to correction for off-resonance effects and subject movement in diffusion MR imaging. *NeuroImage*. https://doi.org/10.1016/j.neuroimage.2015.10.019

Barbas, H. (2015). General Cortical and Special Prefrontal Connections: Principles from Structure to Function. *Annual Review of Neuroscience*, *38*(1), 269–289. https://doi.org/10.1146/annurev-neuro-071714-033936

Barnett, A. J., Reilly, W., Dimsdale-zucker, H., Mizrak, E., Reagh, Z., & Barnett, A. J. (2020). Organization of cortico-hippocampal networks in the human brain, 1–30.

Behrens, T. E. J., Berg, H. J., Jbabdi, S., Rushworth, M. F. S., & Woolrich, M. W. (2007). Probabilistic diffusion tractography with multiple fibre orientations: What can we gain? *NeuroImage*, *34*(1), 144–155. https://doi.org/10.1016/j.neuroimage.2006.09.018

Blondel, V. D., Guillaume, J. L., Lambiotte, R., & Lefebvre, E. (2008). Fast unfolding of communities in large networks. *Journal of Statistical Mechanics: Theory and Experiment*. https://doi.org/10.1088/1742-5468/2008/10/P10008

Brown, J. A., Rudie, J. D., Bandrowski, A., Van Horn, J. D., & Bookheimer, S. Y. (2012). The UCLA multimodal connectivity database: A web-based platform for brain connectivity matrix sharing and analysis. *Frontiers in Neuroinformatics*, *6*(NOV), 1–17. https://doi.org/10.3389/fninf.2012.00028

Burns, S. (2014). A Recipe for Cortical Tractography Using Freesufer Labels. Retrieved February 14, 2020, from

http://sburns.org/2014/05/03/cortical-tractography-recipe.html
Burt, J. B., Demirtaş, M., Eckner, W. J., Navejar, N. M., Ji, J. L., Martin, W. J., … Murray, J. D. (2018). Hierarchy of transcriptomic specialization across human cortex captured by structural neuroimaging topography. *Nature Neuroscience*, *21*(September). https://doi.org/10.1038/s41593-018-0195-0
Chan, A. M., Dykstra, A. R., Jayaram, V., Leonard, M. K., Travis, K. E., Gygi, B., … Cash, S. S. (2014). Speech-specific tuning of neurons in human superior temporal gyrus. *Cerebral Cortex*, *24*(10), 2679–2693. https://doi.org/10.1093/cercor/bht127
Cheng, Q., Roth, A., Halgren, E., & Mayberry, R. I. (2019). Effects of Early Language Deprivation on Brain Connectivity: Language Pathways in Deaf Native and Late First-Language Learners of American Sign Language. *Frontiers in Human Neuroscience*, *13*(September), 1–12. https://doi.org/10.3389/fnhum.2019.00320
Coalson, T., Van Essen, D., & Glasser, M. (2016). *hcp-users FAQ #9: How do I map data between FreeSurfer and HCP?*
Dayan, P., & Abbott, L. F. (2001). Theoretical neuroscience: computational and mathematical modeling of neural systems.
Desikan, R. S., Ségonne, F., Fischl, B., Quinn, B. T., Dickerson, B. C., Blacker, D., … Killiany, R. J. (2006). An automated labeling system for subdividing the human cerebral cortex on MRI scans into gyral based regions of interest. *NeuroImage*, *31*(3), 968–980. https://doi.org/10.1016/j.neuroimage.2006.01.021
Dick, A. S., & Tremblay, P. (2012). Beyond the arcuate fasciculus: Consensus and controversy in the connectional anatomy of language. *Brain*. https://doi.org/10.1093/brain/aws222
Donahue, C. J., Sotiropoulos, S. N., Jbabdi, S., Hernandez-Fernandez, M., Behrens, T. E., Dyrby, T. B., … Glasser, M. F. (2016). Using Diffusion Tractography to Predict Cortical Connection Strength and Distance: A Quantitative Comparison with Tracers in the Monkey. *Journal of Neuroscience*, *36*(25), 6758–6770. https://doi.org/10.1523/JNEUROSCI.0493-16.2016
Eichert, N., Verhagen, L., Folloni, D., Jbabdi, S., Khrapitchev, A. A., Sibson, N. R., … Mars, R. B. (2019). What is special about the human arcuate fasciculus? Lateralization, projections, and expansion. *Cortex*. https://doi.org/10.1016/j.cortex.2018.05.005
Ercsey-Ravasz, M., Markov, N. T., Lamy, C., VanEssen, D. C., Knoblauch, K., Toroczkai, Z., & Kennedy, H. (2013). A Predictive Network Model of Cerebral Cortical Connectivity Based on a Distance Rule. *Neuron*, *80*(1), 184–197. https://doi.org/10.1016/j.neuron.2013.07.036
Felleman, D. J., & Van Essen, D. C. (1991). Distributed Hierarchical Processing in the Primate Cerebral Cortex. *Cerebral Cortex*, *1*(1), 1–47. https://doi.org/10.1093/cercor/1.1.1
Fischl, B. (2012). FreeSurfer. *NeuroImage*. https://doi.org/10.1016/j.neuroimage.2012.01.021
Fischl, B., Sereno, M. I., Tootell, R. B. H., & Dale, A. M. (1999). High-resolution intersubject averaging and a coordinate system for the cortical surface. *Human Brain Mapping*, *8*(4), 272–284. https://doi.org/10.1002/(SICI)1097-0193(1999)8:4<272::AID-HBM10>3.0.CO;2-4
Fischl, B., Van Der Kouwe, A., Destrieux, C., Halgren, E., Ségonne, F., Salat, D. H., … Dale, A. M. (2004). Automatically Parcellating the Human Cerebral Cortex. *Cerebral Cortex*, *14*(1), 11–22. https://doi.org/10.1093/cercor/bhg087
Gershon, R. C., Wagster, M. V, Hendrie, H. C., Fox, N. A., Cook, K. F., & Nowinski, C. J. (2013). NIH toolbox for assessment of neurological and behavioral function. *Neurology*, *80*(11 Supplement 3), S2–S6.
Glasser, M. F., Coalson, T. S., Robinson, E. C., Hacker, C. D., Harwell, J., Yacoub, E., … Van Essen, D. C. (2016a). A multi-modal parcellation of human cerebral cortex. *Nature*, *536*(7615), 171–178. https://doi.org/10.1038/nature18933
Glasser, M. F., Coalson, T. S., Robinson, E. C., Hacker, C. D., Harwell, J., Yacoub, E., … Van Essen, D. C. (2016b). A multi-modal parcellation of human cerebral cortex. *Nature*, *536*(7615), 171–178. https://doi.org/10.1038/nature18933
Glasser, M. F., & Van Essen, D. C. (2011). Mapping Human Cortical Areas In Vivo Based on Myelin Content as Revealed by T1- and T2-Weighted MRI. *Journal of Neuroscience*, *31*(32), 11597–11616. https://doi.org/10.1523/JNEUROSCI.2180-11.2011
Hagler, D. J., Ahmadi, M. E., Kuperman, J., Holland, D., McDonald, C. R., Halgren, E., & Dale, A. M. (2009). Automated white-matter tractography using a probabilistic diffusion tensor atlas: Application to temporal lobe epilepsy. *Human Brain Mapping*, *30*(5), 1535–1547. https://doi.org/10.1002/hbm.20619
Hagmann, P. (2005). *From diffusion MRI to brain connectomics*. EPFL.
Hagmann, P., Cammoun, L., Gigandet, X., Meuli, R., Honey, C. J., Van Wedeen, J., & Sporns, O. (2008). Mapping the structural core of human cerebral cortex. *PLoS Biology*, *6*(7), 1479–1493. https://doi.org/10.1371/journal.pbio.0060159
Honey, C. J., Sporns, O., Cammoun, L., Gigandet, X., Thiran, J. P., Meuli, R., & Hagmann, P. (2009). Predicting human resting-state functional connectivity from structural connectivity. *Proceedings of the National Academy of Sciences of the United States of America*, *106*(6), 2035–2040. https://doi.org/10.1073/pnas.0811168106
Humphries, M. D., & Gurney, K. (2008). Network "small-world-ness": A quantitative method for determining canonical network equivalence. *PLoS ONE*. https://doi.org/10.1371/journal.pone.0002051
Jenkinson, M., Beckmann, C. F., Behrens, T. E. J., Woolrich, M. W., & Smith, S. M. (2012). FSL. *NeuroImage*, *62*(2), 782–790. https://doi.org/10.1016/j.neuroimage.2011.09.015
Jeurissen, B., Descoteaux, M., Mori, S., & Leemans, A. (2019). Diffusion MRI fiber tractography of the brain. *NMR in Biomedicine*, *32*(4), 1–22. https://doi.org/10.1002/nbm.3785
Ji, J. L., Spronk, M., Kulkarni, K., Repovš, G., Anticevic, A., & Cole, M. W. (2019). Mapping the human brain's cortical-subcortical functional network organization. *NeuroImage*, *185*(September 2018), 35–57. https://doi.org/10.1016/j.neuroimage.2018.10.006

Larson-Prior, L. J., Oostenveld, R., Della Penna, S., Michalareas, G., Prior, F., Babajani-Feremi, A., … Snyder, A. Z. (2013). Adding dynamics to the Human Connectome Project with MEG. *NeuroImage*, *80*, 190–201. https://doi.org/10.1016/j.neuroimage.2013.05.056

Latora, V., & Marchiori, M. (2001). Efficient behavior of small-world networks. *Physical Review Letters*. https://doi.org/10.1103/PhysRevLett.87.198701

Lebel, C., & Beaulieu, C. (2011). Longitudinal development of human brain wiring continues from childhood into adulthood. *Journal of Neuroscience*, *31*(30), 10937–10947.

Lennie, P. (2003). The cost of cortical computation. *Current Biology*, *13*(6), 493–497.

Liewald, D., Miller, R., Logothetis, N., Wagner, H. J., & Schüz, A. (2014). Distribution of axon diameters in cortical white matter: an electron-microscopic study on three human brains and a macaque. *Biological Cybernetics*, *108*(5), 541–557. https://doi.org/10.1007/s00422-014-0626-2

Marcus, D. S., Harwell, J., Olsen, T., Hodge, M., Glasser, M. F., Prior, F., … Van Essen, D. C. (2011). Informatics and data mining tools and strategies for the human connectome project. *Frontiers in Neuroinformatics*, *5*(June), 1–12. https://doi.org/10.3389/fninf.2011.00004

Markov, N. T., Ercsey-Ravasz, M. M., Ribeiro Gomes, A. R., Lamy, C., Magrou, L., Vezoli, J., … Kennedy, H. (2014). A weighted and directed interareal connectivity matrix for macaque cerebral cortex. *Cerebral Cortex*, *24*(1), 17–36. https://doi.org/10.1093/cercor/bhs270

Markov, N. T., Ercsey-Ravasz, M., Van Essen, D. C., Knoblauch, K., Toroczkai, Z., & Kennedy, H. (2013). Cortical High-Density Counterstream Architectures. *Science*, *342*(6158), 1238406–1238406. https://doi.org/10.1126/science.1238406

Markov, Nikola T., Vezoli, J., Chameau, P., Falchier, A., Quilodran, R., Huissoud, C., … Kennedy, H. (2014). Anatomy of hierarchy: Feedforward and feedback pathways in macaque visual cortex. *Journal of Comparative Neurology*, *522*(1), 225–259. https://doi.org/10.1002/cne.23458

Mori, S., Crain, B. J., Chacko, V. P., & Van Zijl, P. C. M. (1999). Three-dimensional tracking of axonal projections in the brain by magnetic resonance imaging. *Annals of Neurology: Official Journal of the American Neurological Association and the Child Neurology Society*, *45*(2), 265–269.

Mori, S., Oishi, K., Jiang, H., Jiang, L., Li, X., Akhter, K., … Mazziotta, J. (2008). Stereotaxic white matter atlas based on diffusion tensor imaging in an ICBM template. *NeuroImage*, *40*(2), 570–582. https://doi.org/10.1016/j.neuroimage.2007.12.035

Mount, C. W., & Monje, M. (2017). Wrapped to adapt: experience-dependent myelination. *Neuron*, *95*(4), 743–756.

Muller, L., Chavane, F., Reynolds, J., & Sejnowski, T. J. (2018). Cortical travelling waves: mechanisms and computational principles. *Nature Reviews Neuroscience*. https://doi.org/10.1038/nrn.2018.20

Newman, M. E. J. (2003). The structure and function of complex networks. *SIAM Review*. https://doi.org/10.1137/S003614450342480

Newman, M. E. J. (2004). Fast algorithm for detecting community structure in networks. *Physical Review E*, *69*(6), 66133.

Panesar, S. S., Yeh, F.-C., Jacquesson, T., Hula, W., & Fernandez-Miranda, J. C. (2018). A quantitative tractography study into the connectivity, segmentation and laterality of the human inferior longitudinal fasciculus. *Frontiers in Neuroanatomy*, *12*, 47.

Romeo, R. R., Segaran, J., Leonard, J. A., Robinson, S. T., West, M. R., Mackey, A. P., … Gabrieli, J. D. E. (2018). Language exposure relates to structural neural connectivity in childhood. *Journal of Neuroscience*, *38*(36), 7870–7877.

Rubinov, M., & Sporns, O. (2010). Complex network measures of brain connectivity: Uses and interpretations. *NeuroImage*. https://doi.org/10.1016/j.neuroimage.2009.10.003

Sotiropoulos, S. N., Jbabdi, S., Xu, J., Andersson, J. L., Moeller, S., Auerbach, E. J., … Behrens, T. E. J. (2013). Advances in diffusion MRI acquisition and processing in the Human Connectome Project. *NeuroImage*, *80*, 125–143. https://doi.org/10.1016/j.neuroimage.2013.05.057

Sporns, O., Tononi, G., & Kötter, R. (2005). The human connectome: A structural description of the human brain. *PLoS Computational Biology*, *1*(4), 0245–0251. https://doi.org/10.1371/journal.pcbi.0010042

Theodoni, P., Majka, P., Reser, D. H., Wójcik, D. K., Rosa, M. G. P., & Wang, X.-J. (2020). Structural attributes and principles of the neocortical connectome in the marmoset monkey. *BioRxiv*.

Tournier, J. D., Smith, R., Raffelt, D., Tabbara, R., Dhollander, T., Pietsch, M., … Connelly, A. (2019). MRtrix3: A fast, flexible and open software framework for medical image processing and visualisation. *NeuroImage*, *202*(January), 116137. https://doi.org/10.1016/j.neuroimage.2019.116137

Trebaul, L., Deman, P., Tuyisenge, V., Jedynak, M., Hugues, E., Rudrauf, D., … David, O. (2018). Probabilistic functional tractography of the human cortex revisited. *NeuroImage*, *181*(January), 414–429. https://doi.org/10.1016/j.neuroimage.2018.07.039

Van Essen, D. C., Smith, S. M., Barch, D. M., Behrens, T. E. J., Yacoub, E., & Ugurbil, K. (2013). The WU-Minn Human Connectome Project: An overview. *NeuroImage*, *80*, 62–79. https://doi.org/10.1016/j.neuroimage.2013.05.041

Van Essen, D. C., & Ugurbil, K. (2017). Components of the Human Connectome Project - Diffusion Tractography. Retrieved May 3, 2020, from https://www.humanconnectome.org/study/hcp-young-adult/project-protocol/diffusion-tractography

Ventura-Antunes, L., Mota, B., & Herculano-Houzel, S. (2013). Different scaling of white matter volume, cortical connectivity, and gyrification across rodent and primate brains. *Frontiers in Neuroanatomy*, *7*(MARCH), 1–12.

https://doi.org/10.3389/fnana.2013.00003
von Keyserlingk Graf, D., & Schramm, U. (1984). Diameter of axons and thickness of myelin sheaths of the pyramidal tract fibres in the adult human medullary pyramid. *Anatomischer Anzeiger*, *157*(2), 97–111.
Wang, S. S. H., Shultz, J. R., Burish, M. J., Harrison, K. H., Hof, P. R., Towns, L. C., … Wyatt, K. D. (2008). Functional trade-offs in white matter axonal scaling. *Journal of Neuroscience*, *28*(15), 4047–4056. https://doi.org/10.1523/JNEUROSCI.5559-05.2008
Watts, D. J., & Strogatz, S. H. (1998). Collective dynamics of 'small-world'networks. *Nature*, *393*(6684), 440.
Yeh, F. C., Panesar, S., Fernandes, D., Meola, A., Yoshino, M., Fernandez-Miranda, J. C., … Verstynen, T. (2018). Population-averaged atlas of the macroscale human structural connectome and its network topology. *NeuroImage*, *178*(January), 57–68. https://doi.org/10.1016/j.neuroimage.2018.05.027
Yeh, F. C., Verstynen, T. D., Wang, Y., Fernández-Miranda, J. C., & Tseng, W. Y. I. (2013). Deterministic diffusion fiber tracking improved by quantitative anisotropy. *PLoS ONE*, *8*(11), 1–16. https://doi.org/10.1371/journal.pone.0080713
Yendiki, A. (2017). TRACULA. Retrieved March 11, 2020, from http://surfer.nmr.mgh.harvard.edu/pub/docs/tracula,fs.ppt
Yendiki, A., Panneck, P., Srinivasan, P., Stevens, A., Zöllei, L., Augustinack, J., … Fischl, B. (2011). Automated probabilistic reconstruction of white-matter pathways in health and disease using an atlas of the underlying anatomy. *Frontiers in Neuroinformatics*, *5*(October), 1–12. https://doi.org/10.3389/fninf.2011.00023
Zhang, K., & Sejnowski, T. J. (2000). A universal scaling law between gray matter and white matter of cerebral cortex. *Proceedings of the National Academy of Sciences of the United States of America*, *97*(10), 5621–5626. https://doi.org/10.1073/pnas.090504197

Supplementary Materials

Distribution of connection strengths

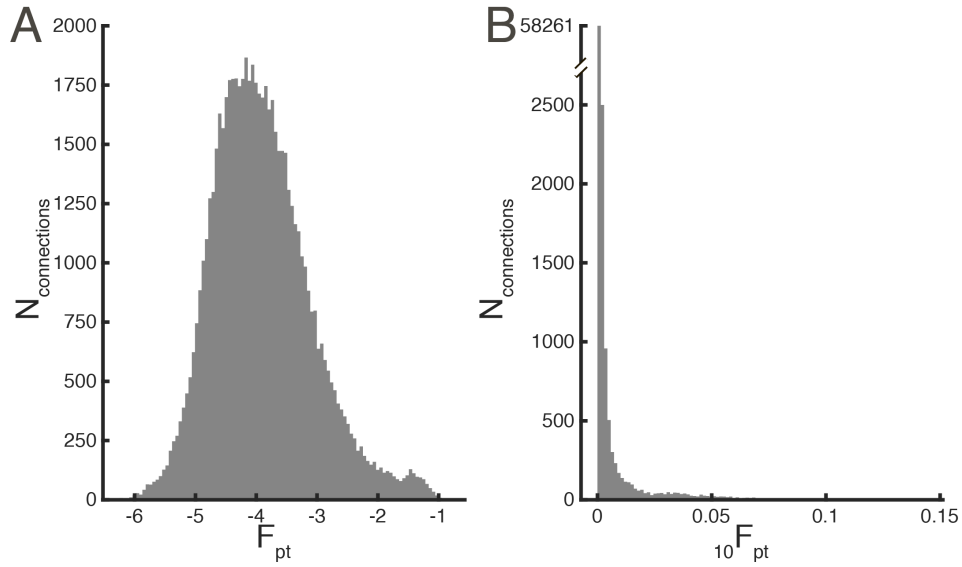

Figure S1. Distribution of pairwise connection strengths. (**A**) $\log_{10}$ transformed value (**B**) pre-transformed values.

Quantification of subject motion

Part of the dMRI preprocessing performed on the WU-Minn HCP data set is correction for eddy currents and movement with FSL eddy (Andersson & Sotiropoulos, 2016). Subjects' estimated displacement over time from their initial position is written to the eddy_restricted_movement_rms output. A scalar index of each subject's motion was derived by integrating their displacement over time, see figure S2.

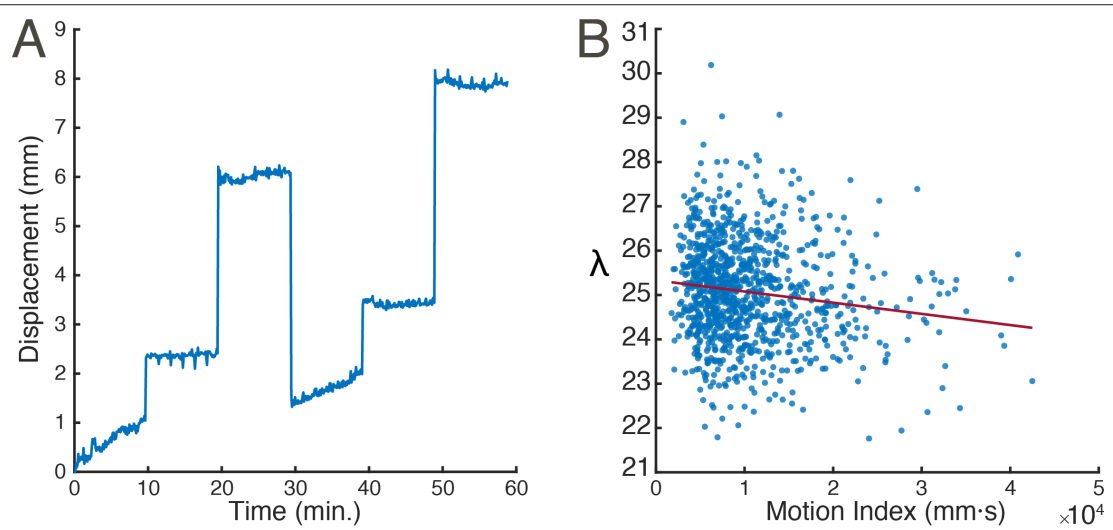

Figure S2. Effect of motion during the dMRI scan. (**A**) Time-course of displacement relative to initial position for one subject (996782). The six runs of the HCP dMRI protocol can be seen. (**B**) Exponential fall-off coefficient λ is only modestly affected by motion, r = 0.140. Each marker represents a subject.

Myelination Difference Connectome

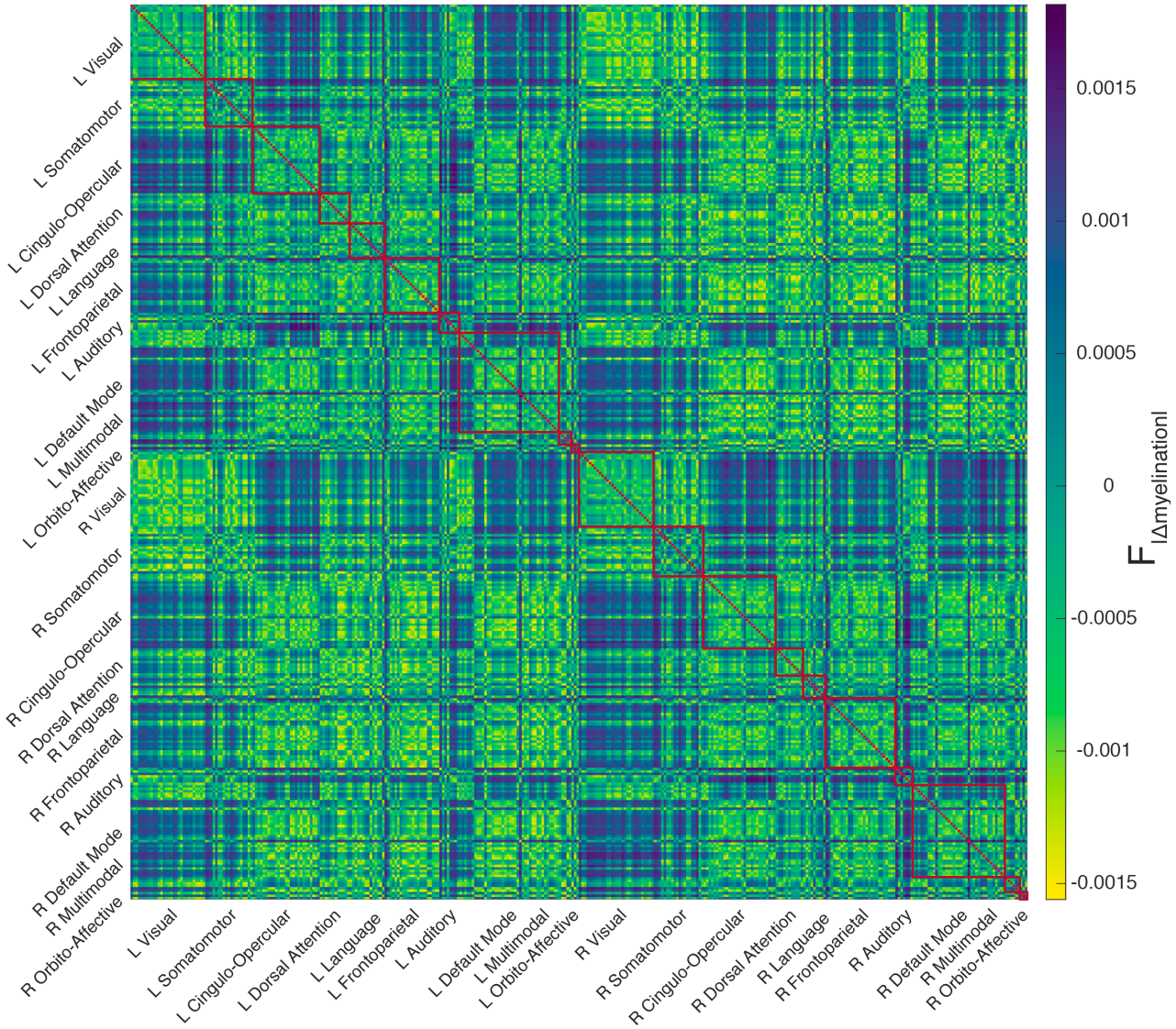

Figure S3. Myelination difference connectivity matrix. This provides an estimate for the difference in hierarchical level between cortical parcels. Values have been fractionally scaled. Note that the color scale has been reversed when compared to Fig. 1, as |Δmyelination| is inversely proportional to connectivity.

Supplementary tables

Idx.	Parcel	F_{pt} to contra-lateral homolog	Mean [$CI_{95\%}$] F_{pt} to non-homologous contra-lateral parcels	Idx.	Parcel	F_{pt} to contra-lateral homolog	Mean [$CI_{95\%}$] F_{pt} to non-homologous contra-lateral parcels	Idx.	Parcel	F_{pt} to contra-lateral homolog	Mean [$CI_{95\%}$] F_{pt} to non-homologous contra-lateral parcels
1	V1	-1.69	-3.72 [-3.88 -3.57]	**61**	46	-1.57	-4.15 [-4.39 -3.90]	**121**	IP1	-2.92	-4.14 [-4.31 -3.99]
2	ProS	-4.87	-4.71 [-4.81 -4.60]	**62**	9-46d	-1.66	-3.92 [-4.12 -3.70]	**122**	PFm	-3.63	-4.09 [-4.19 -3.99]
3	DVT	-2.49	-3.97 [-4.11 -3.83]	**63**	43	-1.38	-3.65 [-3.82 -3.46]	**123**	p10p	-4.75	-4.51 [-4.59 -4.43]
4	MST	-1.98	-3.86 [-4.01 -3.73]	**64**	PFcm	-1.70	-4.23 [-4.43 -3.99]	**124**	p47r	-3.80	-4.33 [-4.46 -4.19]
5	V6	-2.31	-3.95 [-4.10 -3.81]	**65**	PoI2	-1.35	-4.09 [-4.30 -3.87]	**125**	A1	-4.16	-4.49 [-4.59 -4.38]
6	V2	-3.18	-4.25 [-4.39 -4.09]	**66**	FOP4	-5.19	-5.06 [-5.19 -4.91]	**126**	52	-4.07	-4.37 [-4.50 -4.24]
7	V3	-3.90	-4.62 [-4.74 -4.49]	**67**	MI	-2.18	-3.94 [-4.11 -3.75]	**127**	RI	-4.26	-4.50 [-4.62 -4.38]
8	V4	-1.66	-3.80 [-4.00 -3.61]	**68**	FOP1	-3.14	-4.45 [-4.62 -4.30]	**128**	TA2	-4.60	-4.62 [-4.74 -4.52]
9	V8	-2.48	-3.89 [-4.04 -3.72]	**69**	FOP3	-1.38	-3.60 [-3.78 -3.43]	**129**	PBelt	-4.84	-4.80 [-4.92 -4.70]
10	V3A	-2.14	-4.17 [-4.35 -4.00]	**70**	PFop	-2.06	-3.84 [-3.99 -3.67]	**130**	MBelt	-4.68	-4.67 [-4.77 -4.52]
11	V7	-3.17	-4.58 [-4.74 -4.38]	**71**	PF	-2.52	-4.09 [-4.23 -3.93]	**131**	LBelt	-3.10	-3.91 [-4.04 -3.80]
12	IPS1	-2.43	-4.14 [-4.28 -3.99]	**72**	PoI1	-1.67	-3.78 [-3.93 -3.62]	**132**	A4	-4.46	-4.47 [-4.60 -4.37]
13	FFC	-2.64	-4.05 [-4.18 -3.89]	**73**	FOP5	-2.67	-4.18 [-4.33 -4.00]	**133**	7m	-3.89	-4.21 [-4.32 -4.10]
14	V3B	-1.88	-3.69 [-3.83 -3.52]	**74**	PI	-2.93	-4.17 [-4.32 -4.01]	**134**	POS1	-3.94	-4.29 [-4.40 -4.19]
15	LO1	-2.11	-3.51 [-3.64 -3.37]	**75**	a32pr	-3.53	-4.20 [-4.31 -4.08]	**135**	23d	-4.01	-4.28 [-4.41 -4.17]
16	LO2	-3.71	-4.43 [-4.55 -4.32]	**76**	p24	-4.24	-4.43 [-4.56 -4.30]	**136**	v23ab	-4.25	-4.42 [-4.52 -4.29]
17	PIT	-3.59	-4.30 [-4.43 -4.18]	**77**	PEF	-2.49	-4.04 [-4.17 -3.88]	**137**	d23ab	-4.26	-4.34 [-4.44 -4.24]
18	MT	-3.83	-4.37 [-4.49 -4.27]	**78**	7PL	-2.85	-4.23 [-4.37 -4.08]	**138**	31pv	-4.08	-4.28 [-4.38 -4.18]
19	LIPv	-4.33	-4.60 [-4.70 -4.46]	**79**	MIP	-4.13	-4.86 [-5.00 -4.69]	**139**	a24	-4.84	-4.80 [-4.91 -4.70]
20	VIP	-3.77	-4.56 [-4.69 -4.42]	**80**	LIPd	-4.77	-5.06 [-5.21 -4.91]	**140**	d32	-5.15	-4.81 [-4.91 -4.70]
21	PH	-3.62	-4.39 [-4.51 -4.26]	**81**	6a	-3.03	-4.41 [-4.57 -4.27]	**141**	p32	-5.17	-4.71 [-4.80 -4.61]
22	V6A	-3.72	-4.46 [-4.59 -4.34]	**82**	PFt	-3.09	-4.31 [-4.47 -4.16]	**142**	10r	-2.54	-3.96 [-4.09 -3.80]
23	VMV1	-4.55	-4.60 [-4.71 -4.50]	**83**	AIP	-2.38	-4.13 [-4.31 -3.98]	**143**	47m	-3.55	-4.15 [-4.25 -4.03]
24	VMV3	-4.69	-4.75 [-4.88 -4.63]	**84**	PHA3	-2.53	-4.12 [-4.27 -3.95]	**144**	8Av	-4.12	-4.56 [-4.69 -4.44]
25	V4t	-3.63	-4.30 [-4.42 -4.18]	**85**	TE2p	-2.68	-4.13 [-4.29 -3.97]	**145**	8Ad	-3.30	-4.14 [-4.26 -4.02]
26	FST	-1.86	-3.65 [-3.81 -3.49]	**86**	PHT	-2.64	-4.21 [-4.34 -4.03]	**146**	9m	-3.76	-4.35 [-4.47 -4.24]
27	V3CD	-1.75	-3.53 [-3.67 -3.38]	**87**	PGp	-2.30	-3.98 [-4.12 -3.83]	**147**	8BL	-3.46	-4.42 [-4.54 -4.27]
28	LO3	-4.28	-4.52 [-4.64 -4.40]	**88**	IP0	-1.38	-3.89 [-4.06 -3.70]	**148**	9p	-2.89	-4.00 [-4.14 -3.89]
29	VMV2	-2.00	-3.57 [-3.68 -3.44]	**89**	55b	-2.57	-4.18 [-4.33 -4.06]	**149**	10d	-3.06	-4.00 [-4.14 -3.89]
30	VVC	-1.73	-3.58 [-3.75 -3.41]	**90**	PSL	-2.31	-3.99 [-4.13 -3.82]	**150**	47l	-4.84	-4.69 [-4.81 -4.58]
31	4	-2.67	-3.96 [-4.10 -3.80]	**91**	SFL	-3.67	-4.39 [-4.49 -4.27]	**151**	9a	-3.42	-4.06 [-4.16 -3.96]
32	3b	-1.64	-4.06 [-4.26 -3.87]	**92**	STV	-4.67	-4.85 [-5.01 -4.72]	**152**	10v	-2.96	-4.13 [-4.25 -4.00]
33	5m	-1.84	-3.90 [-4.07 -3.72]	**93**	44	-1.99	-4.15 [-4.30 -3.92]	**153**	10pp	-3.53	-4.67 [-4.81 -4.53]
34	5L	-1.64	-3.98 [-4.17 -3.77]	**94**	45	-4.67	-4.70 [-4.82 -4.56]	**154**	OFC	-4.15	-4.79 [-4.92 -4.67]
35	24dd	-2.12	-4.05 [-4.23 -3.81]	**95**	IFJa	-4.00	-4.53 [-4.65 -4.42]	**155**	47s	-4.32	-4.61 [-4.73 -4.50]
36	24dv	-1.94	-3.82 [-3.98 -3.65]	**96**	IFSp	-2.78	-4.24 [-4.41 -4.07]	**156**	EC	-4.04	-4.49 [-4.61 -4.38]
37	7AL	-2.49	-3.85 [-3.98 -3.69]	**97**	STGa	-2.52	-4.22 [-4.37 -4.04]	**157**	PreS	-4.41	-4.44 [-4.55 -4.34]
38	7PC	-2.47	-3.86 [-4.04 -3.70]	**98**	A5	-2.82	-4.37 [-4.54 -4.21]	**158**	H	-3.82	-4.48 [-4.60 -4.33]
39	1	-2.02	-3.59 [-3.75 -3.46]	**99**	STSda	-4.16	-4.62 [-4.76 -4.49]	**159**	PHA1	-3.97	-4.43 [-4.56 -4.32]
40	2	-1.92	-3.90 [-4.06 -3.67]	**100**	STSdp	-4.44	-4.65 [-4.76 -4.53]	**160**	STSvp	-4.14	-4.75 [-4.87 -4.62]
41	3a	-2.40	-4.17 [-4.36 -3.97]	**101**	TPOJ1	-4.95	-4.80 [-4.92 -4.68]	**161**	TGd	-2.32	-3.85 [-4.01 -3.66]
42	6d	-2.06	-3.50 [-3.60 -3.38]	**102**	TGv	-5.82	-5.08 [-5.21 -4.97]	**162**	TE1a	-1.99	-3.89 [-4.07 -3.68]
43	6mp	-1.57	-3.67 [-3.84 -3.42]	**103**	RSC	-4.49	-4.43 [-4.52 -4.33]	**163**	TE2a	-3.62	-4.48 [-4.61 -4.37]
44	6v	-2.03	-3.82 [-3.97 -3.66]	**104**	POS2	-4.43	-4.67 [-4.80 -4.54]	**164**	PGi	-1.55	-4.22 [-4.41 -4.02]
45	OP4	-1.97	-3.41 [-3.55 -3.27]	**105**	7Pm	-4.01	-4.48 [-4.59 -4.34]	**165**	PGs	-1.51	-4.34 [-4.55 -4.07]
46	OP1	-2.65	-3.76 [-3.87 -3.65]	**106**	8BM	-4.18	-4.21 [-4.33 -4.09]	**166**	PHA2	-2.16	-4.17 [-4.33 -4.02]
47	OP2-3	-2.69	-3.90 [-4.01 -3.78]	**107**	8C	-4.46	-4.46 [-4.57 -4.36]	**167**	31pd	-4.05	-4.16 [-4.25 -4.05]
48	FOP2	-3.04	-4.07 [-4.17 -3.94]	**108**	a47r	-4.41	-4.52 [-4.67 -4.39]	**168**	31a	-5.76	-5.07 [-5.17 -4.94]
49	Ig	-2.55	-3.74 [-3.85 -3.64]	**109**	IFJp	-4.91	-4.65 [-4.77 -4.52]	**169**	25	-5.26	-4.79 [-4.89 -4.66]
50	FEF	-3.14	-4.16 [-4.26 -4.05]	**110**	IFSa	-3.04	-4.09 [-4.23 -3.94]	**170**	s32	-2.53	-4.13 [-4.26 -3.97]
51	5mv	-2.32	-3.83 [-3.96 -3.69]	**111**	p9-46v	-5.51	-4.88 [-5.00 -4.76]	**171**	STSva	-2.92	-4.24 [-4.40 -4.07]
52	23c	-2.37	-3.82 [-4.00 -3.67]	**112**	a9-46v	-4.75	-4.48 [-4.59 -4.36]	**172**	TE1m	-3.81	-4.16 [-4.25 -4.04]
53	SCEF	-2.75	-4.18 [-4.31 -4.03]	**113**	a10p	-4.71	-4.76 [-4.90 -4.60]	**173**	PCV	-4.43	-4.49 [-4.60 -4.37]
54	6ma	-1.95	-4.03 [-4.17 -3.88]	**114**	11l	-5.68	-5.03 [-5.17 -4.88]	**174**	TPOJ2	-4.09	-4.50 [-4.60 -4.37]
55	7Am	-1.68	-3.79 [-3.93 -3.64]	**115**	13l	-6.03	-5.14 [-5.26 -5.04]	**175**	TPOJ3	-3.63	-4.26 [-4.36 -4.14]
56	p24pr	-2.72	-4.32 [-4.49 -4.13]	**116**	i6-8	-3.63	-4.61 [-4.74 -4.48]	**176**	PeEc	-4.70	-4.66 [-4.77 -4.55]
57	33pr	-1.78	-4.08 [-4.26 -3.85]	**117**	s6-8	-4.15	-4.68 [-4.81 -4.56]	**177**	TF	-4.35	-4.48 [-4.57 -4.37]
58	a24pr	-2.02	-4.11 [-4.35 -3.87]	**118**	AVI	-3.84	-4.27 [-4.40 -4.15]	**178**	Pir	-4.41	-4.34 [-4.43 -4.23]
59	p32pr	-1.92	-4.06 [-4.27 -3.84]	**119**	TE1p	-3.35	-4.09 [-4.23 -3.96]	**179**	AAIC	-1.93	-4.01 [-4.19 -3.82]
60	6r	-1.97	-3.98 [-4.21 -3.76]	**120**	IP2	-3.10	-4.00 [-4.11 -3.88]	**180**	pOFC	-1.76	-4.03 [-4.25 -3.80]

Table S1. Differential connectivity between contralateral homologous parcels vs the mean of all other contralateral parcels. Confidence intervals are Bonferroni-corrected for multiple comparisons.

Idx.	Parcel	r	p	Idx.	Parcel	r	p	Idx.	Parcel	r	p
1	V1	0.07	n.s.	**61**	46	-0.31	7.18E-07	**121**	IP1	0.12	n.s.
2	ProS	0.15	n.s.	**62**	9-46d	-0.31	4.04E-07	**122**	PFm	0.04	n.s.
3	DVT	0.23	3.99E-03	**63**	43	0.00	n.s.	**123**	p10p	-0.33	2.77E-08
4	MST	0.06	n.s.	**64**	PFcm	0.03	n.s.	**124**	p47r	-0.26	2.51E-04
5	V6	0.20	n.s.	**65**	Pol2	-0.03	n.s.	**125**	A1	0.05	n.s.
6	V2	0.09	n.s.	**66**	FOP4	-0.14	n.s.	**126**	52	0.06	n.s.
7	V3	0.12	n.s.	**67**	MI	-0.12	n.s.	**127**	RI	0.01	n.s.
8	V4	0.12	n.s.	**68**	FOP1	-0.06	n.s.	**128**	TA2	0.05	n.s.
9	V8	0.08	n.s.	**69**	FOP3	-0.10	n.s.	**129**	PBelt	0.10	n.s.
10	V3A	0.15	n.s.	**70**	PFop	0.05	n.s.	**130**	MBelt	0.08	n.s.
11	V7	0.16	n.s.	**71**	PF	0.05	n.s.	**131**	LBelt	0.07	n.s.
12	IPS1	0.17	n.s.	**72**	Pol1	-0.01	n.s.	**132**	A4	0.10	n.s.
13	FFC	0.12	n.s.	**73**	FOP5	-0.10	n.s.	**133**	7m	-0.05	n.s.
14	V3B	0.16	n.s.	**74**	PI	-0.02	n.s.	**134**	POS1	0.07	n.s.
15	LO1	0.15	n.s.	**75**	a32pr	-0.30	2.60E-06	**135**	23d	-0.12	n.s.
16	LO2	0.12	n.s.	**76**	p24	-0.27	6.33E-05	**136**	v23ab	-0.08	n.s.
17	PIT	0.12	n.s.	**77**	PEF	-0.16	n.s.	**137**	d23ab	-0.10	n.s.
18	MT	0.05	n.s.	**78**	7PL	0.13	n.s.	**138**	31pv	-0.13	n.s.
19	LIPv	0.06	n.s.	**79**	MIP	0.14	n.s.	**139**	a24	-0.31	1.12E-06
20	VIP	0.08	n.s.	**80**	LIPd	0.08	n.s.	**140**	d32	-0.34	1.23E-08
21	PH	0.10	n.s.	**81**	6a	-0.11	n.s.	**141**	p32	-0.35	4.09E-09
22	V6A	0.20	4.92E-02	**82**	PFt	0.07	n.s.	**142**	10r	-0.36	4.05E-10
23	VMV1	0.09	n.s.	**83**	AIP	0.07	n.s.	**143**	47m	-0.16	n.s.
24	VMV3	0.08	n.s.	**84**	PHA3	0.11	n.s.	**144**	8Av	-0.21	2.27E-02
25	V4t	0.09	n.s.	**85**	TE2p	0.08	n.s.	**145**	8Ad	-0.30	3.27E-06
26	FST	0.08	n.s.	**86**	PHT	0.03	n.s.	**146**	9m	-0.38	4.11E-11
27	V3CD	0.17	n.s.	**87**	PGp	0.13	n.s.	**147**	8BL	-0.35	2.80E-09
28	LO3	0.11	n.s.	**88**	IP0	0.17	n.s.	**148**	9p	-0.33	4.18E-08
29	VMV2	0.06	n.s.	**89**	55b	-0.10	n.s.	**149**	10d	-0.37	1.90E-10
30	VVC	0.13	n.s.	**90**	PSL	0.03	n.s.	**150**	47l	-0.15	n.s.
31	4	0.02	n.s.	**91**	SFL	-0.29	1.00E-05	**151**	9a	-0.33	3.62E-08
32	3b	0.04	n.s.	**92**	STV	0.03	n.s.	**152**	10v	-0.34	2.60E-08
33	5m	0.01	n.s.	**93**	44	-0.21	2.25E-02	**153**	10pp	-0.26	3.45E-04
34	5L	0.04	n.s.	**94**	45	-0.18	n.s.	**154**	OFC	-0.28	3.28E-05
35	24dd	-0.09	n.s.	**95**	IFJa	-0.17	n.s.	**155**	47s	-0.19	n.s.
36	24dv	-0.16	n.s.	**96**	IFSp	-0.24	1.01E-03	**156**	EC	0.02	n.s.
37	7AL	0.04	n.s.	**97**	STGa	-0.03	n.s.	**157**	PreS	0.01	n.s.
38	7PC	0.06	n.s.	**98**	A5	0.07	n.s.	**158**	H	0.06	n.s.
39	1	0.06	n.s.	**99**	STSda	0.04	n.s.	**159**	PHA1	0.07	n.s.
40	2	0.06	n.s.	**100**	STSdp	-0.01	n.s.	**160**	STSvp	-0.04	n.s.
41	3a	0.05	n.s.	**101**	TPOJ1	0.00	n.s.	**161**	TGd	-0.11	n.s.
42	6d	-0.05	n.s.	**102**	TGv	-0.03	n.s.	**162**	TE1a	-0.04	n.s.
43	6mp	-0.03	n.s.	**103**	RSC	-0.03	n.s.	**163**	TE2a	-0.02	n.s.
44	6v	-0.09	n.s.	**104**	POS2	0.11	n.s.	**164**	PGi	0.01	n.s.
45	OP4	0.06	n.s.	**105**	7Pm	0.00	n.s.	**165**	PGs	0.06	n.s.
46	OP1	0.03	n.s.	**106**	8BM	-0.37	1.14E-10	**166**	PHA2	0.08	n.s.
47	OP2-3	-0.01	n.s.	**107**	8C	-0.22	1.25E-02	**167**	31pd	-0.13	n.s.
48	FOP2	-0.06	n.s.	**108**	a47r	-0.25	4.75E-04	**168**	31a	-0.09	n.s.
49	Ig	-0.02	n.s.	**109**	IFJp	-0.17	n.s.	**169**	25	-0.27	9.02E-05
50	FEF	-0.07	n.s.	**110**	IFSa	-0.25	3.91E-04	**170**	s32	-0.34	2.28E-08
51	5mv	-0.07	n.s.	**111**	p9-46v	-0.28	2.50E-05	**171**	STSva	0.02	n.s.
52	23c	-0.12	n.s.	**112**	a9-46v	-0.30	1.33E-06	**172**	TE1m	-0.05	n.s.
53	SCEF	-0.20	n.s.	**113**	a10p	-0.30	2.32E-06	**173**	PCV	-0.07	n.s.
54	6ma	-0.13	n.s.	**114**	11l	-0.18	n.s.	**174**	TPOJ2	0.02	n.s.
55	7Am	0.01	n.s.	**115**	13l	-0.19	n.s.	**175**	TPOJ3	0.04	n.s.
56	p24pr	-0.18	n.s.	**116**	i6-8	-0.16	n.s.	**176**	PeEc	0.02	n.s.
57	33pr	-0.18	n.s.	**117**	s6-8	-0.27	5.76E-05	**177**	TF	0.08	n.s.
58	a24pr	-0.26	2.99E-04	**118**	AVI	-0.13	n.s.	**178**	Pir	-0.16	n.s.
59	p32pr	-0.26	1.58E-04	**119**	TE1p	0.01	n.s.	**179**	AAIC	-0.18	n.s.
60	6r	-0.14	n.s.	**120**	IP2	0.06	n.s.	**180**	pOFC	-0.24	1.58E-03

Table S2. Pearson correlations between the F_{pt} from each left hemisphere parcel to all others and the target parcels' myelination indices. p values are Bonferroni-corrected for multiple comparisons.

Idx.	Parcel	r	p	Idx.	Parcel	r	p	Idx.	Parcel	r	p
181	R_V1	0.08	n.s.	**241**	R_46	-0.29	1.20E-05	**301**	R_IP1	0.13	n.s.
182	R_ProS	0.12	n.s.	**242**	R_9-46d	-0.29	7.49E-06	**302**	R_PFm	0.02	n.s.
183	R_DVT	0.23	2.52E-03	**243**	R_43	0.00	n.s.	**303**	R_p10p	-0.30	2.07E-06
184	R_MST	0.11	n.s.	**244**	R_PFcm	0.05	n.s.	**304**	R_p47r	-0.21	1.69E-02
185	R_V6	0.20	n.s.	**245**	R_PoI2	0.03	n.s.	**305**	R_A1	0.06	n.s.
186	R_V2	0.10	n.s.	**246**	R_FOP4	-0.12	n.s.	**306**	R_52	0.12	n.s.
187	R_V3	0.13	n.s.	**247**	R_MI	-0.08	n.s.	**307**	R_RI	0.03	n.s.
188	R_V4	0.14	n.s.	**248**	R_FOP1	-0.07	n.s.	**308**	R_TA2	0.09	n.s.
189	R_V8	0.09	n.s.	**249**	R_FOP3	-0.08	n.s.	**309**	R_PBelt	0.12	n.s.
190	R_V3A	0.18	n.s.	**250**	R_PFop	0.07	n.s.	**310**	R_MBelt	0.09	n.s.
191	R_V7	0.19	n.s.	**251**	R_PF	0.05	n.s.	**311**	R_LBelt	0.08	n.s.
192	R_IPS1	0.20	n.s.	**252**	R_PoI1	0.09	n.s.	**312**	R_A4	0.15	n.s.
193	R_FFC	0.15	n.s.	**253**	R_FOP5	-0.05	n.s.	**313**	R_7m	-0.05	n.s.
194	R_V3B	0.18	n.s.	**254**	R_PI	0.08	n.s.	**314**	R_POS1	0.06	n.s.
195	R_LO1	0.19	n.s.	**255**	R_a32pr	-0.29	6.54E-06	**315**	R_23d	-0.10	n.s.
196	R_LO2	0.17	n.s.	**256**	R_p24	-0.27	9.60E-05	**316**	R_v23ab	-0.08	n.s.
197	R_PIT	0.15	n.s.	**257**	R_PEF	-0.15	n.s.	**317**	R_d23ab	-0.10	n.s.
198	R_MT	0.11	n.s.	**258**	R_7PL	0.16	n.s.	**318**	R_31pv	-0.11	n.s.
199	R_LIPv	0.09	n.s.	**259**	R_MIP	0.17	n.s.	**319**	R_a24	-0.28	3.54E-05
200	R_VIP	0.11	n.s.	**260**	R_LIPd	0.08	n.s.	**320**	R_d32	-0.32	2.51E-07
201	R_PH	0.15	n.s.	**261**	R_6a	-0.08	n.s.	**321**	R_p32	-0.35	5.11E-09
202	R_V6A	0.23	4.12E-03	**262**	R_PFt	0.07	n.s.	**322**	R_10r	-0.37	1.63E-10
203	R_VMV1	0.11	n.s.	**263**	R_AIP	0.05	n.s.	**323**	R_47m	-0.07	n.s.
204	R_VMV3	0.10	n.s.	**264**	R_PHA3	0.12	n.s.	**324**	R_8Av	-0.20	n.s.
205	R_V4t	0.14	n.s.	**265**	R_TE2p	0.12	n.s.	**325**	R_8Ad	-0.26	1.58E-04
206	R_FST	0.14	n.s.	**266**	R_PHT	0.09	n.s.	**326**	R_9m	-0.37	2.04E-10
207	R_V3CD	0.19	n.s.	**267**	R_PGp	0.16	n.s.	**327**	R_8BL	-0.35	1.95E-09
208	R_LO3	0.17	n.s.	**268**	R_IP0	0.20	n.s.	**328**	R_9p	-0.31	8.63E-07
209	R_VMV2	0.08	n.s.	**269**	R_55b	-0.08	n.s.	**329**	R_10d	-0.36	3.48E-10
210	R_VVC	0.14	n.s.	**270**	R_PSL	0.05	n.s.	**330**	R_47l	-0.07	n.s.
211	R_4	0.04	n.s.	**271**	R_SFL	-0.22	1.06E-02	**331**	R_9a	-0.30	1.63E-06
212	R_3b	0.06	n.s.	**272**	R_STV	0.04	n.s.	**332**	R_10v	-0.34	1.05E-08
213	R_5m	0.04	n.s.	**273**	R_44	-0.20	n.s.	**333**	R_10pp	-0.24	9.97E-04
214	R_5L	0.06	n.s.	**274**	R_45	-0.12	n.s.	**334**	R_OFC	-0.24	1.10E-03
215	R_24dd	-0.06	n.s.	**275**	R_IFJa	-0.18	n.s.	**335**	R_47s	-0.07	n.s.
216	R_24dv	-0.15	n.s.	**276**	R_IFSp	-0.24	1.75E-03	**336**	R_EC	0.03	n.s.
217	R_7AL	0.07	n.s.	**277**	R_STGa	0.03	n.s.	**337**	R_PreS	0.01	n.s.
218	R_7PC	0.07	n.s.	**278**	R_A5	0.11	n.s.	**338**	R_H	0.07	n.s.
219	R_1	0.07	n.s.	**279**	R_STSda	0.09	n.s.	**339**	R_PHA1	0.09	n.s.
220	R_2	0.07	n.s.	**280**	R_STSdp	0.04	n.s.	**340**	R_STSvp	0.03	n.s.
221	R_3a	0.07	n.s.	**281**	R_TPOJ1	0.03	n.s.	**341**	R_TGd	-0.07	n.s.
222	R_6d	-0.03	n.s.	**282**	R_TGv	0.03	n.s.	**342**	R_TE1a	0.01	n.s.
223	R_6mp	-0.01	n.s.	**283**	R_RSC	-0.05	n.s.	**343**	R_TE2a	0.02	n.s.
224	R_6v	-0.08	n.s.	**284**	R_POS2	0.12	n.s.	**344**	R_PGi	0.03	n.s.
225	R_OP4	0.07	n.s.	**285**	R_7Pm	0.03	n.s.	**345**	R_PGs	0.08	n.s.
226	R_OP1	0.04	n.s.	**286**	R_8BM	-0.35	1.71E-09	**346**	R_PHA2	0.08	n.s.
227	R_OP2-3	0.00	n.s.	**287**	R_8C	-0.21	1.51E-02	**347**	R_31pd	-0.12	n.s.
228	R_FOP2	-0.05	n.s.	**288**	R_a47r	-0.23	3.49E-03	**348**	R_31a	-0.09	n.s.
229	R_Ig	0.00	n.s.	**289**	R_IFJp	-0.15	n.s.	**349**	R_25	-0.24	1.61E-03
230	R_FEF	-0.05	n.s.	**290**	R_IFSa	-0.21	3.22E-02	**350**	R_s32	-0.32	1.37E-07
231	R_5mv	-0.04	n.s.	**291**	R_p9-46v	-0.27	8.34E-05	**351**	R_STSva	0.08	n.s.
232	R_23c	-0.09	n.s.	**292**	R_a9-46v	-0.28	2.20E-05	**352**	R_TE1m	0.02	n.s.
233	R_SCEF	-0.16	n.s.	**293**	R_a10p	-0.25	8.16E-04	**353**	R_PCV	-0.05	n.s.
234	R_6ma	-0.08	n.s.	**294**	R_11l	-0.13	n.s.	**354**	R_TPOJ2	0.06	n.s.
235	R_7Am	0.04	n.s.	**295**	R_13l	-0.11	n.s.	**355**	R_TPOJ3	0.08	n.s.
236	R_p24pr	-0.17	n.s.	**296**	R_i6-8	-0.13	n.s.	**356**	R_PeEc	0.04	n.s.
237	R_33pr	-0.18	n.s.	**297**	R_s6-8	-0.22	9.03E-03	**357**	R_TF	0.13	n.s.
238	R_a24pr	-0.26	2.39E-04	**298**	R_AVI	-0.03	n.s.	**358**	R_Pir	-0.11	n.s.
239	R_p32pr	-0.25	4.93E-04	**299**	R_TE1p	0.07	n.s.	**359**	R_AAIC	-0.09	n.s.
240	R_6r	-0.14	n.s.	**300**	R_IP2	0.03	n.s.	**360**	R_pOFC	-0.20	3.99E-02

Table S3. Pearson correlations between the F_{pt} from each right hemisphere parcel to all others and the target parcels' myelination indices. p values are Bonferroni-corrected for multiple comparisons.

Network theory metrics

All network theoretic measures were computed in matlab using the Brain Connectivity Toolbox, 2019-03-03 release (Rubinov & Sporns, 2010). It is available at http://www.brain-connectivity-toolbox.net or https://www.nitrc.org/projects/bct. The definitions for the metrics used (for binary and undirected networks) are repeated below.

Precursor measures

$$d_{i,j} = \sum_{a_{u,v} \in g_{i \leftrightarrow j}} a_{u,v}$$

Where $d_{i,j}$ is the shortest path length, a basis for measuring integration, between nodes i and j, N is the set of all nodes in the network, n is the number of nodes, and $a_{u,v}$ is the binarized connectivity between nodes u and v.

$$t_i = \frac{1}{2} \sum_{j,h \in N} a_{i,j} a_{i,h} a_{j,h}$$

Where t_i is the number of triangles, a basis for measuring integration, around node i.

$$k_i = \sum_{j \in \mathrm{N}} a_{i,j}$$

Where k_i is the number of degree, or number of links, connected to node i.

Mean Clustering Coefficient (MCC)

$$C_i = \frac{1}{n} \sum_{i \in \mathrm{N}} \frac{2t_i}{k_i(k_i - 1)'}$$

Where C_i is the clustering coefficient of node i. ($C_i = 0$ for $k_i < 2$), (Watts & Strogatz, 1998).

$$\mathrm{MCC} = \frac{1}{n} \sum_{i \in \mathrm{N}} C_i$$

Characteristic Path Length (CPL)

$$L_i = \frac{1}{n} \sum_{i \in \mathrm{N}} \frac{\sum_{j=1, j \neq i}^{n} d_{i,j}}{n - 1}$$

Where L_i is the number of the average distance between node i and all other nodes, (Watts & Strogatz, 1998).

$$CPL = \frac{1}{n} \sum_{i \in \mathrm{N}} L_i$$

Global Efficiency

$$E_i = \frac{1}{n}\sum_{i\in \mathrm{N}} \frac{\sum_{j\in \mathrm{N}, j\neq i}^{n} d_{i,j}^{-1}}{n-1}$$

Where E_i is the efficiency of node i.

$$E = \frac{1}{n}\sum_{i\in \mathrm{N}} L_i$$

Where E is the global efficiency of the network, (Latora & Marchiori, 2001).

Modularity

$$Q = \frac{1}{l}\sum_{i,k\in \mathrm{N}} \left(a_{i,j} - \frac{k_i k_j}{l}\right)\delta_{m_i,m_j}$$

Where l is the number of links in the network, m_i is module containing node i, $\delta_{m_i,m_j} = 1$ if $m_i = m_j$, and 0 otherwise, and Q is the global efficiency of the network, (Newman, 2004).

Gamma (normalized MCC)

$$\gamma = \frac{MCC}{MCC_{rand}}$$

Where MCC_{rand} is the MCC of a random network of the same statistical makeup.

Lambda (normalized CPL)

$$\lambda = \frac{CPL}{CPL_{rand}}$$

Where CPL_{rand} is the CPL of a random network of the same statistical makeup. Note that this measure is unrelated to the length constant λ.

Small Worldness

$$S = \frac{\gamma}{\lambda}$$

Where S is the network small-worldness (Humphries & Gurney, 2008).

Transitivity

$$T = \frac{\sum_{i \in \mathrm{N}} 2t_i}{\sum_{i \in \mathrm{N}} k_i(k_i - 1)}$$

Where T is the transitivity of the network (Newman, 2003).

Assortativity

$$r = \frac{l^{-1} \sum_{(i,j) \in \mathrm{L}} k_i k_j - \left[l^{-1} \sum_{(i,j) \in \mathrm{L}} \frac{1}{2}\left(k_i + k_j\right) \right]^2}{l^{-1} \sum_{(i,j) \in \mathrm{L}} \frac{1}{2}\left(k_i^2 + k_j^2\right) - \left[l^{-1} \sum_{(i,j) \in \mathrm{L}} \frac{1}{2}\left(k_i + k_j\right) \right]^2}$$

Where L is the set of all links and r is the assortativity coefficient of the network (Newman, 2003).

Raw Density

$$D = \frac{l}{n^2 - n}$$

Where D is the density of the network before thresholding and binarization.